On the Statistical Model of Source Localization based on Range Difference Measurements

Marco Compagnoni[a,*], Roberto Notari[a], Fabio Antonacci[b], Augusto Sarti[b]

[a]*Dipartimento di Matematica, Politecnico di Milano, Piazza Leonardo da Vinci 32, 20133, Milan, Italy*
[b]*Dipartimento di Elettronica Informazione e Bioingegneria, Politecnico di Milano, Piazza Leonardo da Vinci 32, 20133, Milan, Italy*

Abstract

In this work we study the statistical model of source localization based on Range Difference measurements, under the assumption of Gaussian noise on the data. Our analysis is based on a previous work of the same authors concerning the localization in a noiseless scenario. We investigate the case of planar localization of a source using a minimal configuration of three non aligned receivers. We have four curved exponential families corresponding to four different, non disjoint, regions of the feasible set. For each family we solve Maximum Likelihood Estimation (MLE). This requires to find the projection of a point on a set of segments and arcs of ellipse. Then, we perform the analytic study of the localization accuracy. In particular, we give formulas for mean square error and bias of MLE, depending on the displacement vectors. We validate the results through Montecarlo simulations, in a given setup of the receivers. As the set of feasible measurements is a semialgebraic variety, this investigation makes use of techniques from Algebraic Statistics and Information Geometry.

Keywords: Range difference space, Statistical Modeling, Maximum Likelihood Estimation, Information Geometry, Algebraic Statistics
2010 MSC: 13P25, 62Fxx, 62P30, 94A12

1. Introduction

Source localization from the analysis of the signals captured by multiple sensors is a classical research theme in science and engineering. Among the early studies on this subject (dating back to World War II) is the analysis of the two-dimensional LOng RAnge Navigation (LORAN) radio positioning system. LORAN was based on the measurements of time differences of arrival (TDOAs) of synchronized radio signals originated from three distinct known emitters. The method needed hyperbolic charts for determining the position of the receiver [1]. Since then, there has been a proliferation of areas of applications where source localization plays a fundamental role. Among them, we mention radar and sonar technologies; wireless sensor networks; the Global Positioning System (GPS); and robotics.

An important class of source localization techniques is the one based on Range Differences (RD), or pseudoranges. RD-based localization is characterized by:

a) a point $\mathbf{x}$, the source, whose location we want to find;

b) a set of points $\{\mathbf{m_0}, \ldots, \mathbf{m_n}\}$, the sensors, placed at known positions;

c) the RDs of the signals emitted by the source and measured by the receivers as experimental data.

*Corresponding author
Email addresses: `marco.compagnoni@polimi.it` (Marco Compagnoni), `roberto.notari@polimi.it` (Roberto Notari), `fabio.antonacci@polimi.it` (Fabio Antonacci), `augusto.sarti@polimi.it` (Augusto Sarti)

These techniques are particularly popular in audio signal processing, where pseudoranges are usually computed from the measurements of the TDOAs between calibrated and synchronized microphones [2, 3, 4, 5, 6]. Given a constant wave propagation speed, RDs and TDOAs are simply proportional to each other. Therefore, throughout this manuscript we will treat RD and TDOA as synonymous. In other contexts, for example remote sensing, radar and GPS [7, 8], RDs can again be derived from TDOAs [9] or through other approaches such as energy measurements [10]. This is a convenient choice whenever sensors at different positions are not guaranteed to be synchronised, thus keeping the technological issues and the cost of the sensor network at bay.

In the signal processing literature, there are various examples of analysis of localization models based on numerical simulations. For example, a study of the TDOA–based localization for a minimal configuration of sensors (three receivers coplanar with the source) can be found in [11, 12]. Therein, the author makes use of the concept of TDOA space and offers a first description of the feasible set of TDOAs. Given the importance of the topic, in [13, 14, 15] we offered a systematic and comprehensive analytic investigation of the mathematical models behind TDOA–based source localization. Using algebraic and geometric tools, we studied in detail the deterministic model for the minimal TDOA–based localization. In [15], we defined the TDOA map from the physical plane of source locations to the space of TDOA measurements, which completely encodes the noiseless localization model. Then, we described the image of this map, that is the set of feasible noiseless measurements. Finally, we studied the invertibility of the map and, consequently, the existence and uniqueness of the source for any given set of measurements.

As a confirmation of the importance of these topics for applications, in [16] the authors describe the use of TDOA measurements set for TDOA estimation. Similar works have been carried out also for other kinds of measurements. For example, in [17] the authors describe Range–based localization models, while Directions Of Arrival measurements are considered in [18]. However, in real world scenarios, localization techniques are sensitive to measurement noise. As an example, in audio signal processing the measurements are affected by both additive noise and outlier measurements [19, 20]. In order to deal with these problems, it is necessary to go further in the study of the model, and move from deterministic to statistical modeling. A first step towards this goal was taken in [21], where a denoising algorithm was proposed.

In this work, we deeply investigate the statistical properties of the localization model. This is the main novelty of the paper. We will leverage on the results contained in [15] to achieve the following goals:

1. study the statistical model behind TDOA-based localization for the minimal case of three receivers and one coplanar source. We will give particular care to the problem of ambiguity in localization;

2. provide an effective Maximum Likelihood localization technique that, given the range differences and the location of the sensors, computes the source location;

3. develop a technique that, given the sensor locations and an estimate of the measurement error magnitude, predicts the localization error covariance, as well as its bias.

In order to attain the first goal, we use Information Geometry [22][1]. This theoretical framework is particularly suitable for our geometric approach to the localization problem (see also [23] for its use in the context of Range–based localization). Information Geometry also allows us to apply the asymptotic theory of estimation for studying the accuracy of source localization, which is our third goal in the list. We observe that in [24, 25], an asymptotic estimation of the Mean Square Error (MSE) and the bias have already been obtained with different tools. However, in this work we push the boundary further: we will focus on predicting the accuracy of the asymptotic estimation through the analysis of higher order statistics.

As far as the second goal is concerned, it is well known that Maximum Likelihood Estimation (MLE) is optimal from a statistical point of view, as it attains the Cramer-Rao Lower Bound. In the literature MLE algorithms are based on the maximization of the likelihood function, which depends on the unknown

---

[1]Information Geometry is the discipline where probability theory and statistical inference are studied with the techniques of differential geometry. Its founding idea is that probability distributions for a statistical model are points of a Riemannian manifold, whose metric is provided by the Fisher Information metric.

coordinates of the source. However, the nonlinearity and the non-convexity of the likelihood function make it quite difficult to formulate an effective solution. This is why other sub-optimal techniques are mostly used [26, 27, 28, 29, 30, 31, 32, 33]. Our approach to the problem is completely different, as the estimation is performed in the parameter space of the model. We exploit the knowledge on the geometry of the set of feasible measurements for obtaining a (quasi) closed-form solution of MLE. In our framework, MLE is equivalent to finding the solution of the geometric problem of projecting a point onto the set of feasible measurements, according to a suitable Euclidean structure on the measurements space. As proven in [15], the set of feasible measurements is a semi-algebraic variety, therefore our analysis naturally falls within the domain of Algebraic Statistics [34].

Several are the application fields that could benefit from the proposed method. In particular, when the number of available measurements is an issue, one could be interested in predicting the maximum error achievable. For example, this is crucial for GPS localization, where the number of available satellites is bounded and therefore we should resort to minimal information scenarios [35, 36, 37, 38, 39, 40, 41, 42, 43, 31]. However, our contribution can be useful also in other fields, such as in audio signal processing and wireless sensor networks. Although in these contexts the number of sensors to handle is usually larger than the minimum, there are applications where it is convenient to focus on smaller subsets of them. A specific problem in which the use of small subsets of measurements is advantageous is the detection of outliers [44, 33, 45, 20]. This is an important issue in several contexts. For instance, in audio localization the outliers could be due to the presence of interferers and of reverberations and they severely impair the localization accuracy.

The paper is organized as follows. In Section 2, we recount the main results introduced in [15] on the deterministic model for TDOA–based source localization in a minimal sensing scenario. In Section 3 we focus on accurately defining the statistical model. This is a rather delicate task, due to the difficulties that arise from localization ambiguities. In our approach, we choose to consider the model as a composition of four distinct curved exponential families, one for each region where the restriction of the TDOA map is a diffeomorphism between the physical and the measurements spaces. In Section 4 we address the MLE in the measurements space. As mentioned above, this is equivalent to studying the orthogonal projection of a point onto the set of feasible TDOA measurements. Section 5 is devoted to studying the accuracy of source localization via MLE. Our analysis is based on asymptotic statistical inference through the approach of Information Geometry. In particular, we obtain an analytic form for the mean square error and the bias of the MLE. Moreover, in Section 5.2 we propose a method for evaluating the reliability of the asymptotical inference, based on higher-order statistics. Section 6 looks at the problem from a practical standpoint. In Section 6.1 we explicitly describe the MLE algorithm for each one of the four models defined in Section 3. In Section 6.2 we conduct a simulation campaign, aimed at validating our algorithms and conducting an asymptotic error analysis. In Section 6.3 we then give indications on the source localization problem in a real scenario, in which we don't not know in advance which model to use. In Section 7 we briefly discuss the potential impact of this work and draw some conclusions. Finally, in Appendix A we include the Singular code for computing the Cartesian equation of the Mahalanobis degree discriminant of an ellipse, which has a role in the MLE algorithm.

2. The TDOA space and the deterministic model

The TDOA space and the TDOA maps were introduced in [11, 15] for the analysis of TDOA–based source localization with a minimal configuration of three receivers in two dimensions. In this section, we briefly go over the main results of [15, 14], using the same tools and notations. In order to simplify matters, we only describe the case in which the receivers are not collinear. The interested reader can develop a similar statistical analysis for the case of aligned sensors starting from [15].

One of the main mathematical tools used in [15] is the exterior algebra formalism over the three dimensional Minkowski vector space $\mathbb{R}^{2,1}$, which roughly corresponds to the product of the Euclidean physical plane times the real line containing the TDOAs. This instrument is very useful for handling the equations involved in the localization problem. We refer to Appendix A of [15] for an introduction to the subject.

However, in this manuscript it is sufficient to use the exterior algebra formalism over the Euclidean vector space $\mathbb{R}^2$. For the convenience of the reader, here we summarize the main facts for this particular case.

Let V be a 2–dimensional Euclidean vector space and let $B = \{\mathbf{e_1}, \mathbf{e_2}\}$ be an orthonormal basis. With a slight abuse of notation, we identify a vector $\mathbf{v} = v_1\mathbf{e_1} + v_2\mathbf{e_2}$ with its coordinates $(v_1, v_2)^T$. We have three non trivial vector spaces $\wedge^k V$. In more details, we have

$k = 0$: $\wedge^0 V$ is the space of scalars, it has dimension 1 and $\{1\}$ is an orthonormal basis;

$k = 1$: $\wedge^1 V = V$ is the space of vectors, it has dimension 2 and B is an orthonormal basis;

$k = 2$: $\wedge^2 V$ is the space of the 2–forms, it has dimension 1 and $\{\boldsymbol{\omega} = \mathbf{e_1} \wedge \mathbf{e_2}\}$ is an orthonormal basis.

The three spaces $\wedge^0 V, \wedge^1 V, \wedge^2 V$ form the exterior algebra $\wedge V$ over V. The symbol $\wedge$ stays for the exterior product, which is skew–commutative and linear with respect to each factor. We can be very explicit if working in coordinates with respect to the above natural basis. Let $\mathbf{v} = (v_1, v_2)^T$, $\mathbf{w} = (w_1, w_2)^T$ be vectors. Then

$$\mathbf{v} \wedge \mathbf{w} = (v_1 w_2 - v_2 w_1)\,\boldsymbol{\omega} = \det\begin{pmatrix} v_1 & w_1 \\ v_2 & w_2 \end{pmatrix}\boldsymbol{\omega} \in \wedge^2 V.$$

The Hodge operator $*$ defines an isomorphism between each pair of vector spaces $\wedge^k V$ and $\wedge^{2-k} V$, $k = 0, 1, 2$. Also in this case, we can give an explicit definition of $*$ by describing its action on the natural basis:

$$* 1 = \boldsymbol{\omega}, \quad * \mathbf{e_1} = \mathbf{e_2}, \; * \mathbf{e_2} = -\mathbf{e_1}, \quad * \boldsymbol{\omega} = 1.$$

The linearity of $*$ allows us to write $* \mathbf{v} = (-v_2, v_1)^T$, which means that the Hodge operator acting on $\wedge^1 V$ corresponds to the counterclockwise rotation of $\frac{\pi}{2}$. The rotation is represented by the matrix

$$\mathbf{H} = \begin{pmatrix} 0 & -1 \\ 1 & 0 \end{pmatrix}$$

with respect to B, therefore we have $* \mathbf{v} = \mathbf{H} \mathbf{v}$. Finally, we have

$$*(\mathbf{v} \wedge \mathbf{w}) = *((v_1 w_2 - v_2 w_1)\,\boldsymbol{\omega}) = \det\begin{pmatrix} v_1 & w_1 \\ v_2 & w_2 \end{pmatrix}.$$

2.1. The complete TDOA map

Let us fix some ideas and notations that will be useful throughout the manuscript.

a) We identify the physical plane with the Euclidean plane and, after choosing an orthogonal Cartesian coordinate system, with $\mathbb{R}^2$. We use B as the orthonormal basis. Given a vector $\mathbf{v}$, we denote its Euclidean norm $\|\mathbf{v}\|$ with v and the corresponding unit vector with $\tilde{\mathbf{v}} = \frac{\mathbf{v}}{v}$.

b) $\mathbf{m_i} = (x_i, y_i)^T$ is the location of the i–th sensor. We take the indexes $i = 0, 1, 2$ and we assume that the three sensors are in distinct positions. $\mathbf{x}$ is the position of the source.

c) $\mathbf{d_{ji}} = \mathbf{m_j} - \mathbf{m_i}$ is the displacement vector from the sensor $\mathbf{m_i}$ to the sensor $\mathbf{m_j}$, for $i, j = 0, 1, 2$. $\mathbf{d_i}(\mathbf{x}) = \mathbf{x} - \mathbf{m_i}$ is the displacement vector from the sensor $\mathbf{m_i}$ to the source $\mathbf{x}$, for $i = 0, 1, 2$. Furthermore, we name the angles $\varphi_0 = \widehat{\mathbf{d_{10}d_{20}}}$, $\varphi_1 = \widehat{\mathbf{d_{01}d_{21}}}$ and $\varphi_2 = \widehat{\mathbf{d_{02}d_{12}}}$.

d) For notational simplicity, and with no loss of generality, we assume the propagation speed to be equal to 1. Hence, the noiseless TDOAs correspond to the range differences.

In this setting, we define the complete TDOA map as

$$\boldsymbol{\tau_2^*} : \quad \begin{array}{ccc} \mathbb{R}^2 & \longrightarrow & \mathbb{R}^3 \\ \mathbf{x} & \longmapsto & (\tau_{10}(\mathbf{x}), \tau_{20}(\mathbf{x}), \tau_{21}(\mathbf{x}))^T \end{array}, \tag{1}$$

where

$$\tau_{ji}(\mathbf{x}) = d_j(\mathbf{x}) - d_i(\mathbf{x}). \tag{2}$$

4

For every source position $\mathbf{x}$, the function $\tau_{ji}(\mathbf{x})$ gives the value of the noiseless TDOA between the two selected sensors. The resulting target set $\mathbb{R}^3$ of $\boldsymbol{\tau_2^*}$ is referred to as the TDOA space or τ–space. The map $\boldsymbol{\tau_2^*}$ completely defines the deterministic model behind the TDOA based source localization. In particular, its image $\mathrm{Im}(\boldsymbol{\tau_2^*})$ is the set of feasible TDOAs in the τ–space. This means that three noiseless TDOAs define a point $\boldsymbol{\tau^*} = (\tau_{10}, \tau_{20}, \tau_{21})^T \in \mathrm{Im}(\boldsymbol{\tau_2^*})$ and, wherever the map $\boldsymbol{\tau_2^*}$ is invertible, the source position is $\boldsymbol{\tau_2^*}^{-1}(\boldsymbol{\tau^*})$.

In Figure 1 we draw a configuration of source and receivers. We set r_0, r_1, r_2 the lines containing the sensors, according to the convention that the receiver $\mathbf{m_i}$ does not lie on r_i. Up to relabeling the sensors, we can assume that $*(\mathbf{d_{10}} \wedge \mathbf{d_{20}}) > 0$, i.e. $\mathbf{d_{10}}, \mathbf{d_{20}}$ are counterclockwise oriented.
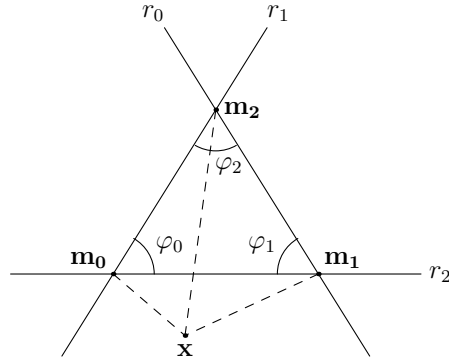

Figure 1: Receivers $\mathbf{m_0}, \mathbf{m_1}, \mathbf{m_2}$ and a source $\mathbf{x}$ in a generic planar configuration.

2.2. The reduced TDOA map

The three range differences that define function 1 are not independent. In fact, the linear relation $\tau_{21}(\mathbf{x}) = \tau_{20}(\mathbf{x}) - \tau_{10}(\mathbf{x})$ holds for each $\mathbf{x} \in \mathbb{R}^2$. This means that three noiseless TDOAs are constrained on the plane

$$\mathcal{H} = \{\boldsymbol{\tau^*} \in \mathbb{R}^3 \mid \tau_{10} - \tau_{20} + \tau_{21} = 0\}. \tag{3}$$

Therefore, we are allowed to choose $\mathbf{m_0}$ as a reference sensor and, without loss of information, to consider only the two TDOAs $\tau_{10}(\mathbf{x}), \tau_{20}(\mathbf{x})$. We define the (reduced) TDOA map:

$$\boldsymbol{\tau_2}: \begin{array}{ccc} \mathbb{R}^2 & \longrightarrow & \mathbb{R}^2 \\ \mathbf{x} & \longmapsto & (\tau_{10}(\mathbf{x}), \tau_{20}(\mathbf{x}))^T \end{array}. \tag{4}$$

Let us consider the projection map $p_3 : \mathbb{R}^3 \to \mathbb{R}^2$ forgetting the third coordinate τ_{21} of the τ–space. Then, we have $\boldsymbol{\tau_2} = p_3 \circ \boldsymbol{\tau_2^*}$ and p_3 is a natural bijection between $\mathrm{Im}(\boldsymbol{\tau_2^*})$ and $\mathrm{Im}(\boldsymbol{\tau_2})$. Hence, we can investigate the properties of the deterministic TDOA model by studying the simpler map $\boldsymbol{\tau_2}$. In analogy with our previous notations, we name τ–plane the target set $\mathbb{R}^2$ of $\boldsymbol{\tau_2}$. To illustrate our exposition, on the left of Figure 2 we draw a configuration of three sensors $\mathbf{m_0} = (0,0)^T$, $\mathbf{m_1} = (2,0)^T$, $\mathbf{m_2} = (2,2)^T$ and three sources $\mathbf{x} = (0.8, 0.8)^T$, $(1.8, -0.4)^T$ and approximately $(2.4, -1.25)^T$. We use this configuration of the sensors in all figures of the manuscript. On the right of Figure 2, we show the image of $\boldsymbol{\tau_2}$ for this choice of receivers and the images of the sources. In Figure 3 we make explicit the relation between $\mathrm{Im}(\boldsymbol{\tau_2})$ and $\mathrm{Im}(\boldsymbol{\tau_2^*})$.

2.2.1. The image of $\boldsymbol{\tau_2}$

$\mathrm{Im}(\boldsymbol{\tau_2})$ is a subset of the convex polytope P_2, which is the hexagon defined by the triangular inequalities:

$$\begin{cases} -d_{10} \leq \tau_{10} \leq d_{10} \\ -d_{20} \leq \tau_{20} \leq d_{20} \\ -d_{21} \leq \tau_{20} - \tau_{10} \leq d_{21} \end{cases}. \tag{5}$$
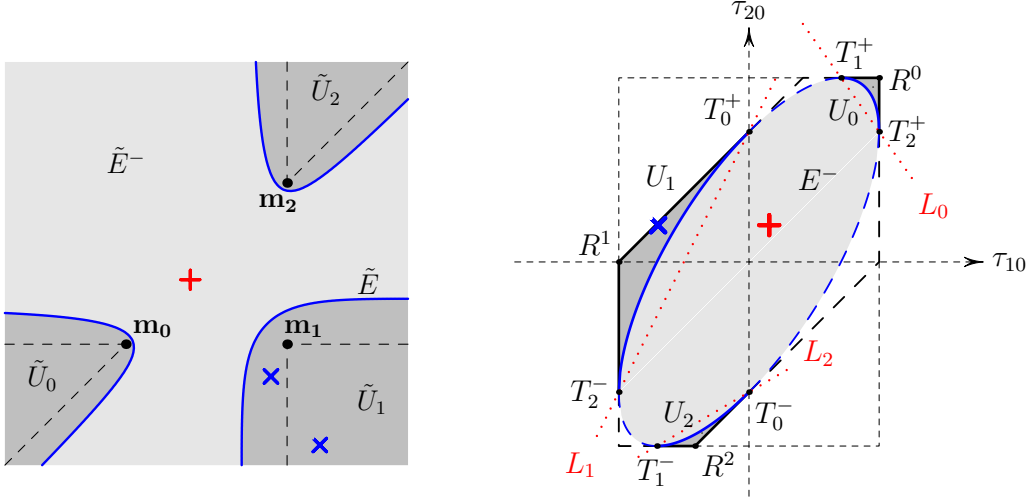
5

Figure 2: On the left, the sensors are the marked points $\mathbf{m_0}, \mathbf{m_1}, \mathbf{m_2}$, while the crosses denote the sources. The curve $\tilde{E}$ separates the light gray region $\tilde{E}^-$ and the medium gray region $\tilde{U}_0 \cup \tilde{U}_1 \cup \tilde{U}_2$. In $\tilde{E}^-$, the map $\boldsymbol{\tau}_2$ is one–to–one and it is possible to locate the source. In $\tilde{U}_0 \cup \tilde{U}_1 \cup \tilde{U}_2$, the map $\boldsymbol{\tau_2}$ is two–to–one and so the localization is not unique. For example, the two blue sources have the same image. On the dashed lines the localization is possible but very sensitive to measurement noise. On the right, there is the image of $\boldsymbol{\tau_2}$. It is the gray subset of the hexagon P_2 with continuous and dashed sides. The light gray region E^- is the image of $\tilde{E}^-$, while each medium gray region U_i is the image of $\tilde{U}_i$. The continuous part of the boundary of the hexagon and the blue ellipse E, together with the vertices R^i, are in the image, and there $\boldsymbol{\tau_2}$ is one–to–one. The points $T_i^{\pm}$ and the dashed boundaries do not belong to $\mathrm{Im}(\boldsymbol{\tau_2})$. Finally, the red dotted lines L_0, L_1, L_2 allow us to single out the medium gray regions U_0, U_1, U_2. The crosses are the images of the sources on the left.

The vertices of P_2 contained in $\mathrm{Im}(\boldsymbol{\tau_2})$ are $R^0 = (d_{10}, d_{20})^T$, $R^1 = (-d_{10}, d_{21} - d_{10})^T$ and $R^2 = (d_{21} - d_{20}, -d_{20})^T$, respectively images of $\mathbf{m_0}$, $\mathbf{m_1}$ and $\mathbf{m_2}$. The other vertices of P_2 are not in the image.

Following the analysis contained in Section 6 of [15], for any $\boldsymbol{\tau} = (\tau_{10}, \tau_{20})^T \in \mathbb{R}^2$ we define the vectors

$$\mathbf{v}(\boldsymbol{\tau}) = *(\tau_{20}\mathbf{d_{10}} - \tau_{10}\mathbf{d_{20}}),$$
$$\mathbf{l_0}(\boldsymbol{\tau}) = \frac{*((d_{20}^2 - \tau_{20}^2)\mathbf{d_{10}} - (d_{10}^2 - \tau_{10}^2)\mathbf{d_{20}})}{2 * (\mathbf{d_{10}} \wedge \mathbf{d_{20}})} \tag{6}$$

and the polynomials

$$a(\boldsymbol{\tau}) = \|\mathbf{v}(\boldsymbol{\tau})\|^2 - *(\mathbf{d_{10}} \wedge \mathbf{d_{20}})^2,$$
$$b(\boldsymbol{\tau}) = \langle \mathbf{v}(\boldsymbol{\tau}), \mathbf{l_0}(\boldsymbol{\tau}) \rangle, \tag{7}$$
$$c(\boldsymbol{\tau}) = \|\mathbf{l_0}(\boldsymbol{\tau})\|^2.$$

The polynomial $c(\boldsymbol{\tau})$ has degree four. Over the reals, it annihilates only at $(\pm d_{10}, \pm d_{20})$. Instead, $b(\boldsymbol{\tau})$ is a degree three polynomial whose zero set is the red curve C in Figure 6. We set C^- (respectively C^+) the region of the τ–plane where $b(\boldsymbol{\tau}) < 0$ (respectively $b(\boldsymbol{\tau}) > 0$). Finally, $a(\boldsymbol{\tau})$ is a degree two polynomial and its zero set is the unique ellipse E that is tangent to each facet of P_2. We name E^- the interior region of the ellipse, where $a(\boldsymbol{\tau}) < 0$, and E^+ the exterior region, where $a(\boldsymbol{\tau}) > 0$. The six points in $E \cap \partial P_2$ are

$$T_i^{\pm} = \left(\pm \langle \mathbf{d_{10}}, \tilde{\mathbf{d}}_{\mathbf{jk}} \rangle, \pm \langle \mathbf{d_{20}}, \tilde{\mathbf{d}}_{\mathbf{jk}} \rangle \right)^T,$$

where $0 \leq i, j, k \leq 2$, $k < j$ and $j, k \neq i$.

Let us now consider the lines L_0, L_1, L_2 passing through the couples of points $\{T_1^+, T_2^+\}$, $\{T_0^+, T_2^-\}$ and
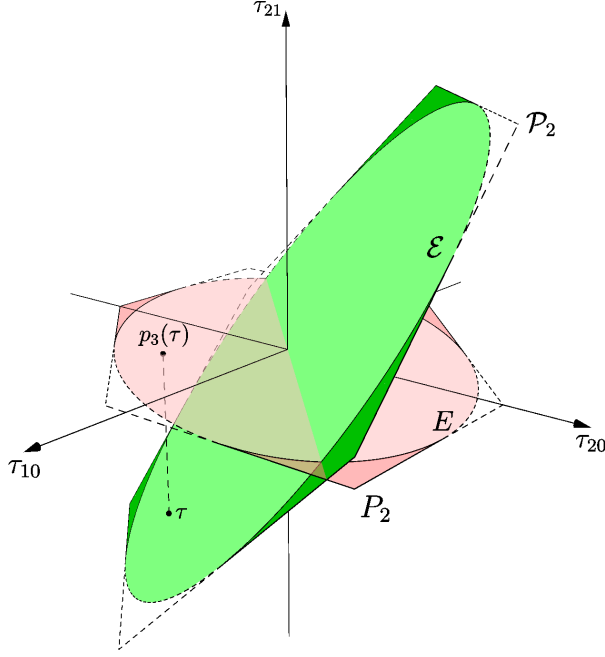
Figure 3: The image of $\boldsymbol{\tau_2^*}$ is the green subset of the hexagon $\mathcal{P}_2 \subset \mathcal{H}$, while the image of $\boldsymbol{\tau_2}$ is the red subset of P_2. There is a one–to–one correspondence between $\mathrm{Im}(\boldsymbol{\tau_2^*})$ and $\mathrm{Im}(\boldsymbol{\tau_2})$ via the projection map p_3. In the lightly shaded regions, the TDOA maps are one–to–one, while in the more darkly shaded regions the maps are two–to–one.

$\{T_0^-, T_1^-\}$, respectively (see Figure 2). They are defined by the vanishing of the three linear forms

$$
\begin{aligned}
l_0(\boldsymbol{\tau}) &= d_{20}\tau_{10} + d_{10}\tau_{20} - d_{10}d_{20}(1 + \cos\varphi_0), \\
l_1(\boldsymbol{\tau}) &= -(d_{10} + d_{21})\tau_{10} + d_{10}\tau_{20} - d_{10}d_{21}(1 + \cos\varphi_1), \\
l_2(\boldsymbol{\tau}) &= d_{20}\tau_{10} - (d_{20} + d_{21})\tau_{20} - d_{20}d_{21}(1 + \cos\varphi_2).
\end{aligned}
\tag{8}
$$

Then, we define the three sets U_i, $i = 0, 1, 2$, as:

$$
U_i = \{\boldsymbol{\tau} \in \mathring{P}_2 \,|\, a(\boldsymbol{\tau}) > 0,\, l_i(\boldsymbol{\tau}) > 0\},
\tag{9}
$$

where $\mathring{P}_2$ is the interior of P_2, that is defined by taking the strict inequalities in (5).

With the above notation, we finally get the image of $\boldsymbol{\tau_2}$:

$$
\mathrm{Im}(\boldsymbol{\tau_2}) = E^- \cup \overline{U}_0 \cup \overline{U}_1 \cup \overline{U}_2 \setminus \{T_0^\pm, T_1^\pm, T_2^\pm\},
\tag{10}
$$

where $\overline{U}_i$ is the closure of U_i with respect to the Euclidean topology. In particular, we have

$$
|\boldsymbol{\tau_2}^{-1}(\boldsymbol{\tau})| = \begin{cases} 2 & \text{if } \boldsymbol{\tau} \in U_0 \cup U_1 \cup U_2, \\ 1 & \text{if } \boldsymbol{\tau} \in \mathrm{Im}(\boldsymbol{\tau_2}) \setminus U_0 \cup U_1 \cup U_2. \end{cases}
\tag{11}
$$

For any given $\boldsymbol{\tau} \in U_0 \cup U_1 \cup U_2$, the two preimages $\mathbf{x}_\pm(\boldsymbol{\tau})$ are given by

$$
\mathbf{x}_\pm(\boldsymbol{\tau}) = \mathbf{m_0} + \mathbf{l_0}(\boldsymbol{\tau}) + \lambda_\pm(\boldsymbol{\tau})\mathbf{v}(\boldsymbol{\tau}),
\tag{12}
$$

where

$$
\lambda_\pm(\boldsymbol{\tau}) = \frac{-b(\boldsymbol{\tau}) \pm \sqrt{b(\boldsymbol{\tau})^2 - a(\boldsymbol{\tau})c(\boldsymbol{\tau})}}{a(\boldsymbol{\tau})}.
\tag{13}
$$

are the solutions of the equation $a(\boldsymbol{\tau})\lambda^2 + 2b(\boldsymbol{\tau})\lambda + c(\boldsymbol{\tau}) = 0$. For $\boldsymbol{\tau} \in \mathrm{Im}(\boldsymbol{\tau_2}) \setminus U_0 \cup U_1 \cup U_2$, we have to take only the $\mathbf{x}_+(\boldsymbol{\tau})$ solution.

7

2.2.2. The situation in the physical plane

In the x–plane there are two main regions. The first one $\tilde{E}^-$ is the preimage of the interior of the ellipse, i.e. $\tilde{E}^- = \boldsymbol{\tau_2}^{-1}(E^-)$. In $\tilde{E}^-$ the TDOA map is one–to–one and the source localization is possible. The second one is the union of the preimages $\tilde{U}_i = \boldsymbol{\tau_2}^{-1}(U_i)$, for $i = 0, 1, 2$. There, the map is two–to–one and there is no way to uniquely locate the source. The transition is on the *bifurcation curve* $\tilde{E} = \boldsymbol{\tau_2}^{-1}(E)$, that consists of three disjoint and unbounded arcs, one for each arc of E contained in $\mathrm{Im}(\boldsymbol{\tau_2})$. As a point $\boldsymbol{\tau}$ in one of the U_i gets close to E, the solution $\mathbf{x}_+(\boldsymbol{\tau})$ gets close to a point on $\tilde{E}$, while $\mathbf{x}_-(\boldsymbol{\tau})$ goes to infinity. The sets $\tilde{E}^-, \tilde{U}_0, \tilde{U}_1, \tilde{U}_2$ are open subsets of the x–plane, separated by the three arcs of $\tilde{E}$.

Finally, let us define the linear forms

$$s_i(\mathbf{x}) = (-1)^i * (\mathbf{d_k}(\mathbf{x}) \wedge \mathbf{d_j}(\mathbf{x})), \tag{14}$$

where i, j, k are different from each other and $0 \le j < k \le 2$. The zero set of $s_i(\mathbf{x})$ is the line r_i, $i = 0, 1, 2$. The union D of the six dashed half–lines originating from the receivers is called *degeneracy locus* of $\boldsymbol{\tau_2}$, i.e. the locus where the rank of the Jacobian matrix of $\boldsymbol{\tau_2}$ drops. D is the zero set of the function

$$s(\mathbf{x}) = d_0(\mathbf{x})\, s_0(\mathbf{x}) + d_1(\mathbf{x})\, s_1(\mathbf{x}) + d_2(\mathbf{x})\, s_2(\mathbf{x}) \tag{15}$$

and it is the preimage of the six straight line segments in $\partial P_2 \cap \mathrm{Im}(\boldsymbol{\tau_2})$. On D we have $\mathbf{x}_+(\boldsymbol{\tau}) = \mathbf{x}_-(\boldsymbol{\tau})$, thus the TDOA map is one–to–one. Furthermore, D divides each $\tilde{U}_i$ into two connected components and $\boldsymbol{\tau_2}$ is a bijection between each of them and the corresponding U_i.

3. The statistical model

In the presence of measurement errors on the data, we must resort to statistical modeling. In this section, we focus on the definition of the statistical models for TDOA–based localization in the minimal planar scenario. As we are going to see, we need to define a plurality of models in order to take care of issues of non-uniqueness in source localization. In particular, we will consider four distinct curved exponential families, corresponding to the four different regions in the x–plane. In our analysis we follow the notation of [22]. This will be particularly useful in Section 5, where we study the source estimation accuracy via the asymptotic analysis techniques given by Information Geometry.

3.1. The complete and the reduced models

In this subsection we adapt the analysis contained in Sections 3 and 4 of [21] to the case of three TDOAs. For sake of completeness, we include in this Section part of the mathematical derivation in [21]. In this manuscript we assume the noise to be Gaussian, therefore the TDOAs associated to a source in $\mathbf{x}$ are described by

$$\hat{\boldsymbol{\tau}}_\mathbf{2}^*(\mathbf{x}) = \boldsymbol{\tau}_\mathbf{2}^*(\mathbf{x}) + \boldsymbol{\epsilon}, \quad \text{where} \quad \boldsymbol{\epsilon} \sim N(\mathbf{0}, \boldsymbol{\Sigma}) \tag{16}$$

and the covariance matrix $\boldsymbol{\Sigma}$ is known and non singular. This is the most common choice in application scenarios [12, 46]. From a mathematical standpoint, this error distribution allows us to use the many existing tools for the study of statistical exponential families. However, our analysis is helpful also in situations where errors are no longer Gaussian, for example in the presence of outliers [20]. We define (16) as the *complete statistical model*. This means that the probability density function (p.d.f.) for the measured TDOAs $\hat{\boldsymbol{\tau}}^* = (\hat{\tau}_{10}, \hat{\tau}_{20}, \hat{\tau}_{21})^T$ is

$$p(\hat{\boldsymbol{\tau}}^*; \boldsymbol{\tau}_\mathbf{2}^*(\mathbf{x}), \boldsymbol{\Sigma}) = \frac{1}{\sqrt{(2\pi)^3 |\boldsymbol{\Sigma}|}} \exp\left[-\frac{1}{2}(\hat{\boldsymbol{\tau}}^* - \boldsymbol{\tau}_\mathbf{2}^*(\mathbf{x}))^T \boldsymbol{\Sigma}^{-1}(\hat{\boldsymbol{\tau}}^* - \boldsymbol{\tau}_\mathbf{2}^*(\mathbf{x}))\right]. \tag{17}$$

From a geometric standpoint, the Fisher matrix $\boldsymbol{\Sigma}^{-1}$ defines a Euclidean structure on the τ–space, with scalar product

$$\langle \mathbf{v_1}, \mathbf{v_2} \rangle_{\boldsymbol{\Sigma}} = \mathbf{v_1}^T \boldsymbol{\Sigma}^{-1} \mathbf{v_2}, \qquad \mathbf{v_1}, \mathbf{v_2} \in \mathbb{R}^3. \tag{18}$$

The associated distance is the Mahalanobis distance

$$\|\mathbf{v}\|_{\boldsymbol{\Sigma}} = \sqrt{\langle \mathbf{v}, \mathbf{v} \rangle_{\boldsymbol{\Sigma}}}, \qquad \mathbf{v} \in \mathbb{R}^3. \tag{19}$$

We can rewrite the p.d.f. (17) as:

$$p(\hat{\boldsymbol{\tau}}^*; \boldsymbol{\tau_2^*}(\mathbf{x}), \boldsymbol{\Sigma}) = \frac{1}{\sqrt{(2\pi)^3 |\boldsymbol{\Sigma}|}} \exp \left[-\frac{1}{2} \|\hat{\boldsymbol{\tau}}^* - \boldsymbol{\tau_2^*}(\mathbf{x}))\|_{\boldsymbol{\Sigma}}^2 \right]. \tag{20}$$

Theorem 1. *Let $\mathcal{P}_{\mathcal{H}}(\hat{\boldsymbol{\tau}}^*; \boldsymbol{\Sigma})$ be the orthogonal projection of $\hat{\boldsymbol{\tau}}^* \in \mathbb{R}^3$ on the plane $\mathcal{H}$ defined by $\tau_{10} - \tau_{20} + \tau_{21} = 0$, with respect to $\langle \ , \ \rangle_{\Sigma}$. Then, $\hat{\boldsymbol{\tau}} = p_3 \circ \mathcal{P}_{\mathcal{H}}(\hat{\boldsymbol{\tau}}^*; \boldsymbol{\Sigma})$ is a sufficient statistic for the underlying parameter* $\mathbf{x}$.

Proof. $\mathcal{P}_{\mathcal{H}}(\hat{\boldsymbol{\tau}}^*; \boldsymbol{\Sigma})$ is a sufficient statistic for $\mathbf{x}$, see Theorem 1 in [21]. Since p_3 is one–to–one between $\mathcal{H}$ and $\mathbb{R}^2$, the claim follows. $\quad\square$

Theorem 1 states that all the information about the source position is contained in $\hat{\boldsymbol{\tau}} \in \mathbb{R}^2$. In order to obtain the p.d.f. for $\hat{\boldsymbol{\tau}}$, we observe that $p_3 \circ \mathcal{P}_{\mathcal{H}}(\boldsymbol{\tau_2^*}(\mathbf{x}); \boldsymbol{\Sigma}) = \boldsymbol{\tau_2}(\mathbf{x})$ and we define $\boldsymbol{\Sigma}_2 = \mathbf{P}\boldsymbol{\Sigma}\mathbf{P}^T$, where $\mathbf{P}$ is the representative matrix of $p_3 \circ \mathcal{P}_{\mathcal{H}}$ with respect to the standard basis of $\mathbb{R}^3$ and $\mathbb{R}^2$ (see [21]). From the general transformation rule for the multivariate normal distributions under linear mapping, it follows:

$$p(\hat{\boldsymbol{\tau}}^*; \boldsymbol{\tau_2^*}(\mathbf{x}), \boldsymbol{\Sigma}) = \frac{1}{2\pi\sqrt{|\boldsymbol{\Sigma_2}|}} \exp \left[-\frac{1}{2} \|\hat{\boldsymbol{\tau}} - \boldsymbol{\tau_2}(\mathbf{x}))\|_{\boldsymbol{\Sigma_2}}^2 \right]. \tag{21}$$

where it appears the Mahalanobis distance defined by $\boldsymbol{\Sigma_2}^{-1}$ on $\mathbb{R}^2$. This means that the analysis of the complete statistical model (16) is equivalent to the analysis of the reduced (2D) TDOA statistical model:

$$\hat{\boldsymbol{\tau}}_2(\mathbf{x}) = \boldsymbol{\tau_2}(\mathbf{x}) + \boldsymbol{\epsilon_2}, \quad \text{where} \quad \boldsymbol{\epsilon_2} \sim N(\mathbf{0}, \boldsymbol{\Sigma_2}). \tag{22}$$

For this reason and without loss of generality, in the rest of the paper we focus on the analysis of (22).

3.2. The restricted models are curved exponential families

We now address the problem of ambiguity in source localization, i.e. the fact that the map $\boldsymbol{\tau_2}$ is not globally invertible. The simplest way to solve this issue is to define distinct statistical models for each of the maximal subsets of the x–plane where $\boldsymbol{\tau_2}$ is injective. Throughout the rest of the manuscript we call these the *restricted models*. In the following proposition we define and study the properties of the above maximal subsets of $\mathbb{R}^2$.

Proposition 2. *In the x–plane, let us consider the subsets*

$$\Omega = \{\mathbf{x} \in \mathbb{R}^2 \,|\, s(\mathbf{x}) < 0\} \qquad and \qquad \Omega_i = \{\mathbf{x} \in \mathbb{R}^2 \,|\, s_j > 0, \, s_k > 0\},$$

where i, j, k are different from each other and $0 \leq i, j, k \leq 2$. Then:

1. *the above subsets are open and disjoint from each other and their union is dense in $\mathbb{R}^2$. In particular, $\mathbb{R}^2 \setminus (\Omega \cup \Omega_0 \cup \Omega_1 \cup \Omega_2) = D$, the degeneracy locus of $\boldsymbol{\tau_2}$;*

2. *the restriction of $\boldsymbol{\tau_2}$ on each subset is differentiable and injective, with $Im(\boldsymbol{\tau_2}|_{\Omega}) = Im(\boldsymbol{\tau_2}) \setminus \partial P_2$ and $Im(\boldsymbol{\tau_2}|_{\Omega_i}) = U_i$, $i = 0, 1, 2$. Furthermore, we have $(\boldsymbol{\tau_2}|_{\Omega})^{-1} = \mathbf{x}_+$ and $(\boldsymbol{\tau_2}|_{\Omega_i})^{-1} = \mathbf{x}_-$, $i = 0, 1, 2$.*

Proof. In the following, we assume that i, j, k are different each other. By using identity $\mathbf{d_{ij}} = \mathbf{d_{ik}} - \mathbf{d_{jk}}$, we have

$$s_i(\mathbf{m_i}) = (-1)^i *(\mathbf{d_k}(\mathbf{m_i}) \wedge \mathbf{d_j}(\mathbf{m_i})) = (-1)^i *(\mathbf{d_{ik}} \wedge \mathbf{d_{ij}}) = - *(\mathbf{d_{10}} \wedge \mathbf{d_{20}}) < 0,$$

for every $i = 0, 1, 2$. As a consequence, Ω_i is the intersection of the two open half–planes bounded by r_j, r_k and not containing $\mathbf{m_j}, \mathbf{m_k}$, respectively (see Figure 4). This implies that $\Omega_i \cap \Omega_j = \emptyset$ if $i \neq j$ and the boundary of $\cup_{i=0}^2 \Omega_i$ is D.

Then, let us consider $s(\mathbf{x})$. From Section 2.2.2, we know that $\partial\Omega = D$. In the interior of the triangle of the sensors, one has $s_i(\mathbf{x}) < 0$ for every $i = 0, 1, 2$ and so also $s(\mathbf{x})$ is negative. By continuity, this implies that $s(\mathbf{x}) < 0$ for every $\mathbf{x}$ in the complement of the closure of $\cup_{i=0}^{2}\Omega_i$. It remains to check that $s(\mathbf{x})$ is positive inside every Ω_i. Since $\{\mathbf{d_{10}}, \mathbf{d_{20}}\}$ is a basis of $\mathbb{R}^2$, we can write $\mathbf{d_i}(\mathbf{x}) = \mathbf{d_0}(\mathbf{x}) - \mathbf{d_{i0}} = c_1(\mathbf{x})\,\mathbf{d_{10}} + c_2(\mathbf{x})\,\mathbf{d_{20}} - \mathbf{d_{i0}}$ for $i = 0, 1, 2$. Thus,

$s_0(\mathbf{x}) = *((c_1(\mathbf{x})\,\mathbf{d_{10}} + (c_2(\mathbf{x}) - 1)\,\mathbf{d_{20}}) \wedge ((c_1(\mathbf{x}) - 1)\,\mathbf{d_{10}} + c_2(\mathbf{x})\,\mathbf{d_{20}})) = (c_1(\mathbf{x}) + c_2(\mathbf{x}) - 1) * (\mathbf{d_{10}} \wedge \mathbf{d_{20}})$,
$s_1(\mathbf{x}) = -*((c_1(\mathbf{x})\,\mathbf{d_{10}} + (c_2(\mathbf{x}) - 1)\,\mathbf{d_{20}}) \wedge (c_1(\mathbf{x})\,\mathbf{d_{10}} + c_2(\mathbf{x})\,\mathbf{d_{20}})) = -c_1(\mathbf{x}) * (\mathbf{d_{10}} \wedge \mathbf{d_{20}})$,
$s_2(\mathbf{x}) = *((c_1(\mathbf{x}) - 1)\,\mathbf{d_{10}} + c_2(\mathbf{x})\,\mathbf{d_{20}})) \wedge (c_1(\mathbf{x})\,\mathbf{d_{10}} + c_2(\mathbf{x})\,\mathbf{d_{20}})) = -c_2(\mathbf{x}) * (\mathbf{d_{10}} \wedge \mathbf{d_{20}})$.

By defining $\tilde{s}(\mathbf{x}) = (c_1(\mathbf{x}) + c_2(\mathbf{x}) - 1)\,d_0(\mathbf{x}) - c_1(\mathbf{x})\,d_1(\mathbf{x}) - c_2(\mathbf{x})\,d_2(\mathbf{x})$, we have $s(\mathbf{x}) = \tilde{s}(\mathbf{x}) * (\mathbf{d_{10}} \wedge \mathbf{d_{20}})$. For the sake of simplicity, from now on we focus on Ω_0, being the other cases analogous. In order to study the sign of $s(\mathbf{x})$ in this set, we perform the asymptotic analysis of the restriction of $\tilde{s}(\mathbf{x})$ to the half–line outgoing from $\mathbf{m_0}$ with direction $\mathbf{w} = -\mathbf{d_{10}} - \mathbf{d_{20}}$. In this situation $\mathbf{x}(t) = \mathbf{m_0} + t\mathbf{w}$ and $c_1(\mathbf{x}(t)) = c_2(\mathbf{x}(t)) = -c\,d_0(\mathbf{x}(t))$, where $t \in [0, +\infty)$ and $c = \frac{1}{\|\mathbf{d_{10}} + \mathbf{d_{20}}\|}$. In the limit $d_0(\mathbf{x}) \to +\infty$, we have

$$
\begin{aligned}
d_i(\mathbf{x}) &= \|\mathbf{d_0}(\mathbf{x}) - \mathbf{d_{i0}}\|^2 = \sqrt{d_0(\mathbf{x})^2 - 2\langle \mathbf{d_0}(\mathbf{x}), \mathbf{d_{i0}}\rangle + d_{i0}{}^2} = \\
&= d_0(\mathbf{x})\sqrt{1 + \frac{1}{d_0(\mathbf{x})}\left(-2\,\langle \tilde{\mathbf{d}}_0(\mathbf{x}), \mathbf{d_{i0}}\rangle + \frac{d_{i0}^2}{d_0(\mathbf{x})}\right)} = \\
&= d_0(\mathbf{x})\left(1 - \frac{\langle \tilde{\mathbf{d}}_0(\mathbf{x}), \mathbf{d_{i0}}\rangle}{d_0(\mathbf{x})} + \frac{d_{i0}{}^2 - \langle \tilde{\mathbf{d}}_0(\mathbf{x}), \mathbf{d_{i0}}\rangle^2}{2d_0(\mathbf{x})^2} + o\left(\frac{1}{d_0(\mathbf{x})^2}\right)\right) = \\
&= d_0(\mathbf{x}) - \langle \tilde{\mathbf{d}}_0(\mathbf{x}), \mathbf{d_{i0}}\rangle + \frac{\langle *\tilde{\mathbf{d}}_0(\mathbf{x}), \mathbf{d_{i0}}\rangle^2}{2d_0(\mathbf{x})} + o\left(\frac{1}{d_0(\mathbf{x})}\right) = \\
&= d_0(\mathbf{x}) - \langle \tilde{\mathbf{d}}_0(\mathbf{x}), \mathbf{d_{i0}}\rangle + \frac{*(\tilde{\mathbf{d}}_0(\mathbf{x}) \wedge \mathbf{d_{i0}})^2}{2d_0(\mathbf{x})} + o\left(\frac{1}{d_0(\mathbf{x})}\right),
\end{aligned}
$$

for every $i = 1, 2$ and $\mathbf{x} \in \mathbb{R}^2$. In the derivation of the formula, we exploited the properties of the Hodge operator and the fact that $\{\tilde{\mathbf{d}}_0(\mathbf{x}), *\tilde{\mathbf{d}}_0(\mathbf{x})\}$ is an orthonormal basis of $\mathbb{R}^2$ (see Appendix A of [15]). We use this equality in $\tilde{s}(\mathbf{x})$. Since $c_1(\mathbf{x})\langle \tilde{\mathbf{d}}_0(\mathbf{x}), \mathbf{d_{10}}\rangle + c_2(\mathbf{x})\langle \tilde{\mathbf{d}}_0(\mathbf{x}), \mathbf{d_{20}}\rangle = \langle \tilde{\mathbf{d}}_0(\mathbf{x}), \mathbf{d_0}(\mathbf{x})\rangle = d_0(\mathbf{x})$, on the half–line $\mathbf{x}(t)$ it results

$$
\lim_{t \to +\infty} \tilde{s}(\mathbf{x}(t)) = \frac{c^2}{2}\left(*(\mathbf{w} \wedge \mathbf{d_{10}})^2 + *(\mathbf{w} \wedge \mathbf{d_{20}})^2\right) = \left(\frac{*(\mathbf{d_{10}} \wedge \mathbf{d_{20}})}{\|\mathbf{d_{10}} + \mathbf{d_{20}}\|}\right)^2 > 0.
$$

By continuity, $s(\mathbf{x})$ is positive on every $\mathbf{x} \in \Omega_0$. The remaining claims of the theorem are consequences of the properties of $\boldsymbol{\tau_2}$ summarized in Section 2. $\qquad\qquad\qquad\qquad\qquad\qquad\qquad\qquad\qquad\qquad\quad\square$

In order to simplify the notations, let us define $U = \mathrm{Im}(\boldsymbol{\tau_2}|_\Omega)$. An explicit description of U follows easily by considering in the τ–plane the cubic curve C defined by equation $b(\boldsymbol{\tau}) = 0$ and the associated open regions C^+ and C^-, defined as $b(\boldsymbol{\tau}) > 0$ and $b(\boldsymbol{\tau}) < 0$ respectively (see Figure 6). From the results in Section 6 of [15], we have:

$$U = \mathring{P}_2 \cap (E^- \cup C^+) = \{\boldsymbol{\tau} \in \mathring{P}_2 \,|\, a(\boldsymbol{\tau}) < 0 \text{ or } b(\boldsymbol{\tau}) > 0\}. \tag{23}$$

In Figure 4 we draw the sets $\Omega, \Omega_0, \Omega_1, \Omega_2$, while in Figure 5 there are their images U and U_i, $i = 0, 1, 2$.

At this point, following [22], we recall the definition of curved exponential family.

Definition 3. *Let $\mathcal{X}$ be a set and $\Theta \subseteq \mathbb{R}^n$ an open subset. An n–dimensional exponential family on $\mathcal{X}$, with parameters $\boldsymbol{\theta} \in \Theta$ and random variables $\mathbf{y} \in \mathcal{X}$, is a set S of probability density functions*

$$p(\mathbf{y}; \boldsymbol{\theta}) = \exp\left[C(\mathbf{y}) + \sum_{i=1}^{n}\theta_i F_i(\mathbf{y}) - \psi(\boldsymbol{\theta})\right],$$

where $\{C, F_1, \ldots, F_n\}$ are $n + 1$ real valued functions on $\mathcal{X}$ and $\psi \in C^\infty(\Theta, \mathbb{R})$.
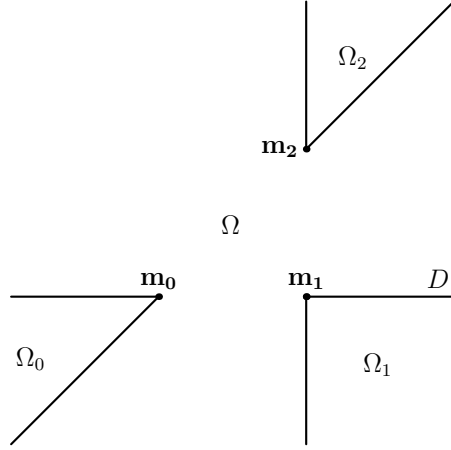
10

Figure 4: $\Omega, \Omega_0, \Omega_1, \Omega_2$ are disjoint open subsets of the x–plane. The closure of their union is $\mathbb{R}^2$, while their boundaries give the discriminacy locus D of $\boldsymbol{\tau_2}$. On each subset the map $\boldsymbol{\tau_2}$ is injective.

Given an exponential family S, the mapping $\phi : S \to \Theta$ given by $\phi(p(\mathbf{y}; \boldsymbol{\theta})) = \boldsymbol{\theta}$ is a global coordinate system of S. By composing ϕ with every C^∞ diffeomorphism of $\mathbb{R}^n$, we obtain a C^∞ atlas on S. This allows us to consider S as a C^∞ differentiable manifold, a so–called *statistical manifold*.

The n–dimensional multivariate normal distribution is an important example of exponential family. Indeed, let $\mathbf{y} \sim N(\boldsymbol{\mu}, \boldsymbol{\Sigma})$. In this context, the probability density function becomes

$$
\begin{aligned}
p(\mathbf{y}; \boldsymbol{\mu}, \boldsymbol{\Sigma}) &= \frac{1}{\sqrt{(2\pi)^n |\boldsymbol{\Sigma}|}} \exp\left[-\frac{1}{2} \|\mathbf{y} - \boldsymbol{\mu}\|_{\boldsymbol{\Sigma}}^2 \right] = \\
&= \exp\left[-\frac{1}{2} \|\mathbf{y}\|_{\boldsymbol{\Sigma}}^2 + \langle \boldsymbol{\mu}, \mathbf{y} \rangle_{\boldsymbol{\Sigma}} - \left(\frac{1}{2} \|\boldsymbol{\mu}\|_{\boldsymbol{\Sigma}}^2 + \log \sqrt{(2\pi)^n |\boldsymbol{\Sigma}|} \right) \right] .
\end{aligned}
\tag{24}
$$

If we assume $\boldsymbol{\Sigma}$ to be known, the only parameters are $\boldsymbol{\theta} = \boldsymbol{\mu}$. By defining

$$
C(\mathbf{y}) = -\frac{1}{2} \|\mathbf{y}\|_{\boldsymbol{\Sigma}}^2, \quad F_i(\mathbf{y}) = (\boldsymbol{\Sigma}^{-1} \mathbf{y})_i, \quad \psi(\boldsymbol{\theta}) = \frac{1}{2} \|\boldsymbol{\theta}\|_{\boldsymbol{\Sigma}}^2 + \log \sqrt{(2\pi)^n |\boldsymbol{\Sigma}|},
$$

the p.d.f. (24) can be rewritten in the canonical form given in Definition 3, where one can identify $\mathcal{X} = \Theta = \mathbb{R}^n$.

Definition 4. *An (n, m) curved exponential family on $\mathcal{X}$ is a set M of probability density functions which forms a smooth m–dimensional submanifold within an n–dimensional exponential family S.*

Now, we can state the main result of this Section.

Theorem 5. *The restriction of the statistical model $\hat{\boldsymbol{\tau}}_{\mathbf{2}}(\mathbf{x})$ on each subset Ω and Ω_i, $i = 0, 1, 2$, is a $(2, 2)$ curved exponential family on $\mathbb{R}^2$, parameterized by $\boldsymbol{\theta}(\mathbf{x}) = \boldsymbol{\tau_2}(\mathbf{x})$.*

Proof. Let us take as S the 2–dimensional exponential family on $\mathcal{X} = \Theta = \mathbb{R}^2$ given by

$$
p(\hat{\boldsymbol{\tau}}; \boldsymbol{\tau_2}, \boldsymbol{\Sigma_2}) = \frac{1}{2\pi \sqrt{|\boldsymbol{\Sigma_2}|}} \exp\left[-\frac{1}{2} \|\hat{\boldsymbol{\tau}} - \boldsymbol{\tau_2}\|_{\boldsymbol{\Sigma_2}}^2 \right],
\tag{25}
$$

where the parameter space is the τ–plane and $\boldsymbol{\theta} = \boldsymbol{\tau_2}$. By Proposition 2, on each subset Ω and Ω_i, $i = 0, 1, 2$, the map $\boldsymbol{\tau_2}(\mathbf{x})$ is a differentiable bijection and defines a 2–dimensional family M of distributions $p(\hat{\boldsymbol{\tau}}; \boldsymbol{\tau_2}(\mathbf{x}), \boldsymbol{\Sigma_2})$ which is smoothly embedded in S. $\qquad \square$
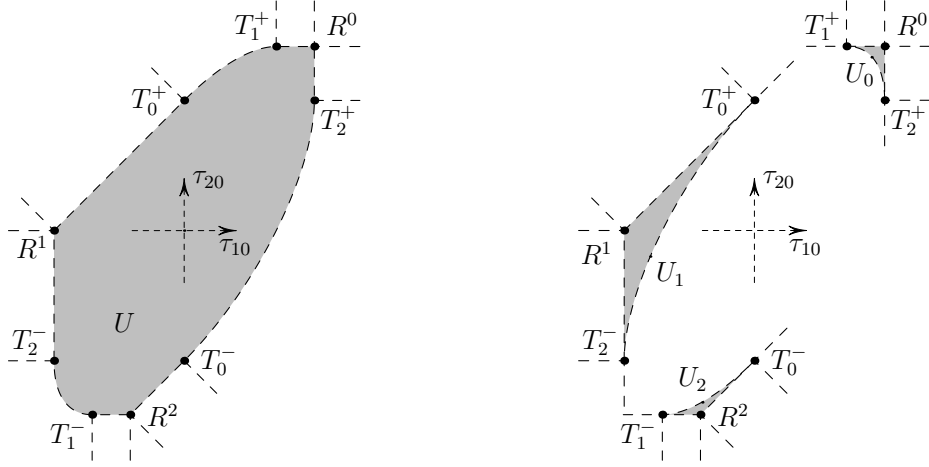
Figure 5: On the left, the medium gray subset is $U = \mathrm{Im}(\boldsymbol{\tau_2}|_\Omega)$. On the right, the medium gray subset having R^i as vertex is $U_i = \mathrm{Im}(\boldsymbol{\tau_2}|_{\Omega_i})$, $i = 0, 1, 2$. The dashes lines subdivide the τ–plane into different regions according to the solution of the Maximum Likelihood Estimator for each restricted model (see Section 4.1).

From now on, we will refer to the curved exponential family defined by $\hat{\boldsymbol{\tau}}_2|_\Omega$ and $\hat{\boldsymbol{\tau}}_2|_{\Omega_i}$, $i = 0, 1, 2$, as M and M_i, respectively, which have the open subsets U and U_i of $\Theta = \mathbb{R}^2$ as parameter spaces (see Figure 5). As said at the beginning of the Section, in the rest of the manuscript we will investigate the properties of the TDOA statistical model through the analysis of the families M, M_0, M_1, M_2.

4. The estimation of the source position in the TDOA space

In this Section we consider the problem of the estimation of the source position in the presence of noisy TDOA measurements. In the literature, the typical approach is based on the optimization of a cost function $f(\mathbf{x}; \hat{\boldsymbol{\tau}}, \boldsymbol{\Sigma})$ in the x–space. The most popular example is Maximum Likelihood Estimation. For a given $\hat{\boldsymbol{\tau}} \in \mathbb{R}^2$, the MLE approach consists in maximizing the likelihood function

$$l(\boldsymbol{\tau_2}(\mathbf{x}); \hat{\boldsymbol{\tau}}, \boldsymbol{\Sigma_2}) = \frac{1}{2\pi\sqrt{|\boldsymbol{\Sigma_2}|}} \exp\left[-\frac{1}{2}\|\hat{\boldsymbol{\tau}} - \boldsymbol{\tau_2}(\mathbf{x})\|^2_{\boldsymbol{\Sigma_2}}\right] .$$

The estimated source location is

$$\bar{\mathbf{x}}(\hat{\boldsymbol{\tau}}; \boldsymbol{\Sigma_2}) = \operatorname*{argmax}_{\mathbf{x}\in\mathbb{R}^2} l(\boldsymbol{\tau_2}(\mathbf{x}); \hat{\boldsymbol{\tau}}, \boldsymbol{\Sigma_2}) = \operatorname*{argmin}_{\mathbf{x}\in\mathbb{R}^2} \|\hat{\boldsymbol{\tau}} - \boldsymbol{\tau_2}(\mathbf{x})\|^2_{\boldsymbol{\Sigma_2}} . \tag{26}$$

It is well know that the MLE is an optimal estimator, as its variance asymptotically attains the Cramer–Rao lower bound. However, finding the solution of the optimization problem (26) is a challenging task. Indeed, the cost function is nonlinear and so it is impossible to find a closed-form solution. On the other hand, when using iterative techniques the solution could get easily trapped in a local minimum, as the cost function is not convex.

Starting from the description of the feasible set of TDOA measurements, we address the source localization problem in a radically different fashion. In the following, we describe step by step how to get a solution for the MLE optimization problem. In Section 6, we code this steps into four algorithms, one for each statistical model.

4.1. The Maximum Likelihood Estimation in the TDOA space

For the sake of simplicity, let us consider the model M. Given $\hat{\boldsymbol{\tau}} \in \mathbb{R}^2$, the Maximum Likelihood Estimation of the TDOAs is $\bar{\boldsymbol{\tau}}(\hat{\boldsymbol{\tau}}; \boldsymbol{\Sigma_2}) = \boldsymbol{\tau_2}(\bar{\mathbf{x}}(\hat{\boldsymbol{\tau}}; \boldsymbol{\Sigma_2}))$, which satisfies

$$\bar{\boldsymbol{\tau}}(\hat{\boldsymbol{\tau}}; \boldsymbol{\Sigma}_2) = \operatorname*{argmin}_{\boldsymbol{\tau}\in U} \|\hat{\boldsymbol{\tau}} - \boldsymbol{\tau}\|^2_{\boldsymbol{\Sigma_2}} . \tag{27}$$

12

This means that, in the τ–plane, an MLE algorithm searches for the point $\bar{\tau}(\hat{\tau}; \Sigma_2) \in U$ at minimum Mahalanobis distance from $\hat{\tau}$. We have two cases. If $\hat{\tau} \in U$, the MLE solution is simply $\bar{\tau}(\hat{\tau}; \Sigma_2) = \hat{\tau}$. On the other hand, if $\hat{\tau} \notin U$, we have to find the closest point to $\hat{\tau}$ on the boundary ∂U of U. In Figure 5, the dashed lines subdivide the τ–plane in several subsets, according to the different types of solution of the MLE for $\Sigma_2 = \sigma^2 I$. In $\mathbb{R}^2 \setminus U$ there are:

a) six regions having the segments of $P_2 \cap \partial U$ as boundaries;

b) three regions having the arcs of $E \cap \partial U$ as boundaries;

c) three angular regions with vertices R^i, $i = 0, 1, 2$.

In the first two subcases, the MLE solution $\bar{\tau}(\hat{\tau}; \Sigma_2)$ is the closest orthogonal projection of $\hat{\tau}$ on the relative boundary of U. In the latter, the MLE solution is the corresponding vertex R^i.

Similar arguments apply also to the models M_i, $i = 0, 1, 2$ and for a generic covariance matrix Σ_2. In particular, for every model it is necessary to compute the projections of $\hat{\tau}$ on $P_2 \cap \bar{U}$ and on the ellipse. The rest of this Section will be focused on the geometric problem of projecting $\hat{\tau}$ on the set of feasible measurements.

4.2. The orthogonal projections on the line segments in $P_2 \cap \partial U$

For a generic point $\hat{\tau} \in \mathbb{R}^2$, there exists a projection $\mathcal{P}_i^{\pm}(\hat{\tau}; \Sigma_2)$ on each of the lines $h_i^{\pm}$, $i = 0, 1, 2$, supporting the six facets of P_2 (see Figure 6).[2] Let us define the vectors $\mathbf{v_0} = (1, 1)^T$, $\mathbf{v_1} = (1, 0)^T$ and $\mathbf{v_2} =$
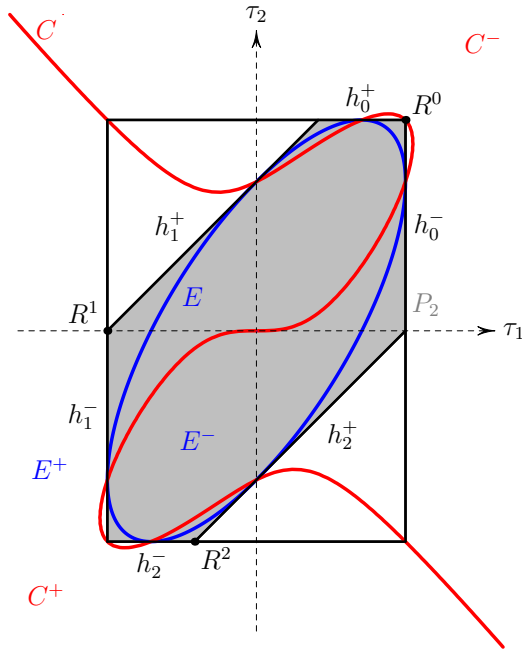
Figure 6: The ellipse E in blue, the cubic C in red and the six lines supporting the facets of P_2. Regions $E^{\pm}$ and $C^{\pm}$ are named according to the sign of $a(\tau)$ and $b(\tau)$ respectively. We note that $U_0, U_1, U_2 \subset C^+$.

---

[2]In order to simplify the exposition, herein we adopt a different notation for the facets of P_2, with respect to the one used in [15]. Indeed, we name $h_i^{\pm}$ the lines supporting two facets containing the vertex R^i, while in [15] we used $F_i^{\pm}$ for the two parallel facets not containing R^i.

$(0, 1)^T$, each one parallel to two facets of P_2. Hence, the points $\mathcal{P}_i^{\pm}(\hat{\boldsymbol{\tau}}; \boldsymbol{\Sigma_2})$, $i = 0, 1, 2$, are:

$$\mathcal{P}_0^+(\hat{\boldsymbol{\tau}}; \boldsymbol{\Sigma_2}) = R^0 + \frac{\langle \hat{\boldsymbol{\tau}} - R^0, \mathbf{v_1} \rangle_{\boldsymbol{\Sigma_2}}}{\|\mathbf{v_1}\|_{\boldsymbol{\Sigma_2}}^2} \mathbf{v_1}, \quad \mathcal{P}_0^-(\hat{\boldsymbol{\tau}}; \boldsymbol{\Sigma_2}) = R^0 + \frac{\langle \hat{\boldsymbol{\tau}} - R^0, \mathbf{v_2} \rangle_{\boldsymbol{\Sigma_2}}}{\|\mathbf{v_2}\|_{\boldsymbol{\Sigma_2}}^2} \mathbf{v_2},$$

$$\mathcal{P}_1^+(\hat{\boldsymbol{\tau}}; \boldsymbol{\Sigma_2}) = R^1 + \frac{\langle \hat{\boldsymbol{\tau}} - R^1, \mathbf{v_0} \rangle_{\boldsymbol{\Sigma_2}}}{\|\mathbf{v_0}\|_{\boldsymbol{\Sigma_2}}^2} \mathbf{v_0}, \quad \mathcal{P}_1^-(\hat{\boldsymbol{\tau}}; \boldsymbol{\Sigma_2}) = R^1 + \frac{\langle \hat{\boldsymbol{\tau}} - R^1, \mathbf{v_2} \rangle_{\boldsymbol{\Sigma_2}}}{\|\mathbf{v_2}\|_{\boldsymbol{\Sigma_2}}^2} \mathbf{v_2}, \qquad (28)$$

$$\mathcal{P}_2^+(\hat{\boldsymbol{\tau}}; \boldsymbol{\Sigma_2}) = R^2 + \frac{\langle \hat{\boldsymbol{\tau}} - R^2, \mathbf{v_0} \rangle_{\boldsymbol{\Sigma_2}}}{\|\mathbf{v_0}\|_{\boldsymbol{\Sigma_2}}^2} \mathbf{v_0}, \quad \mathcal{P}_2^-(\hat{\boldsymbol{\tau}}; \boldsymbol{\Sigma_2}) = R^2 + \frac{\langle \hat{\boldsymbol{\tau}} - R^2, \mathbf{v_1} \rangle_{\boldsymbol{\Sigma_2}}}{\|\mathbf{v_1}\|_{\boldsymbol{\Sigma_2}}^2} \mathbf{v_1}.$$

We need to know which of these projections are in ∂U. To this purpose, we first check if $\mathcal{P}_i^{\pm}(\hat{\boldsymbol{\tau}}; \boldsymbol{\Sigma_2})$ lies on P_2 by verifying inequalities (5). If so, it holds $\mathcal{P}_i^{\pm}(\hat{\boldsymbol{\tau}}; \boldsymbol{\Sigma_2}) \in \partial U$ if and only if $l_i(\mathcal{P}_i^{\pm}(\hat{\boldsymbol{\tau}}; \boldsymbol{\Sigma_2})) \geq 0$, where $l_i(\boldsymbol{\tau})$ are the polynomials (8) defining the lines L_i, $i = 0, 1, 2$.

4.3. The orthogonal projections on the arcs of the ellipse

The projections $\mathcal{P}_E^i(\hat{\boldsymbol{\tau}}; \boldsymbol{\Sigma_2})$, $i = 1, \ldots, k$ of the data point $\hat{\boldsymbol{\tau}} \in \mathbb{R}^2$ on the ellipse E are the stationary points of the squared Mahalanobis distance $\|\hat{\boldsymbol{\tau}} - \boldsymbol{\tau}\|_{\boldsymbol{\Sigma_2}}^2$ restricted to E. Let ν be a Lagrange multiplier and consider the Lagrange function

$$\Lambda(\boldsymbol{\tau}, \nu; \hat{\boldsymbol{\tau}}, \boldsymbol{\Sigma_2}) = \|\hat{\boldsymbol{\tau}} - \boldsymbol{\tau}\|_{\boldsymbol{\Sigma_2}}^2 + \nu\, a(\boldsymbol{\tau}).$$

Consequently $\mathcal{P}_E^i(\hat{\boldsymbol{\tau}}; \boldsymbol{\Sigma_2})$, $i = 1, \ldots, k$ are the real stationary points of $\Lambda(\boldsymbol{\tau}, \nu; \hat{\boldsymbol{\tau}}, \boldsymbol{\Sigma_2})$, i.e. the real solutions of the system

$$\begin{cases} \nabla_{\boldsymbol{\tau}} \Lambda(\boldsymbol{\tau}, \nu; \hat{\boldsymbol{\tau}}, \boldsymbol{\Sigma_2}) = 0 \\ a(\boldsymbol{\tau}) = 0 \end{cases}. \qquad (29)$$

This is a system of polynomial equations that can be solved through symbolic or numerical computation. In the first case, by using elimination theory (see [47]), we can reduce system (29) to a triangular polynomial system. In particular, we obtain a degree four equation in one variable, which admits a closed-form solution. The solutions of the system can then be derived through back–substitution. In doing so, however, we must be careful about issues of numerical stability of the solutions. From a numerical standpoint, in order to solve system (29) we can use some software based on homotopy continuation (e.g. PHCpack [48] or Bertini [49]). In the following paragraph, we propose an alternate approach based on the parametric description of E via trigonometric functions.

Recalling that $\varphi_0 = \widehat{\mathbf{d_{10}}\mathbf{d_{20}}}$, we can state the following:

Proposition 6. *Assume $\gamma \in [0, 2\pi)$. Then*

$$\boldsymbol{\tau}(\gamma) = (d_{10} \sin\gamma, d_{20} \sin(\gamma + \varphi_0))$$

is a one–to–one regular parametrization of E.

Proof. As the Cartesian equation of E is $a(\boldsymbol{\tau}) = 0$, for any given $\boldsymbol{\tau} \in E$ the vector $\mathbf{u}(\boldsymbol{\tau}) = \tau_{20}\mathbf{d_{10}} - \tau_{10}\mathbf{d_{20}}$ satisfies

$$\|\mathbf{u}(\boldsymbol{\tau})\|^2 = \|\tau_{20}\mathbf{d_{10}} - \tau_{10}\mathbf{d_{20}}\|^2 = \|\mathbf{d_{10}} \wedge \mathbf{d_{20}}\|^2.$$

In the x–plane, the vectors $*\mathbf{d_{10}}, *\mathbf{d_{20}}$ are perpendicular to $\mathbf{d_{10}}, \mathbf{d_{20}}$, respectively, therefore $\{\mathbf{d_{10}}, *\mathbf{d_{10}}\}$ and $\{\mathbf{d_{20}}, *\mathbf{d_{20}}\}$ are both orthogonal bases of $\mathbb{R}^2$. This implies that, for any $\boldsymbol{\tau} \in E$, there exists a unique angle $\gamma \in [0, 2\pi)$ such that

$$\mathbf{u}(\boldsymbol{\tau}) = - * (\mathbf{d_{10}} \wedge \mathbf{d_{20}}) (\tilde{\mathbf{d}}_{10} \cos\gamma + *\tilde{\mathbf{d}}_{10} \sin\gamma), \qquad (30)$$

where $\tilde{\mathbf{d}}_{10}, *\tilde{\mathbf{d}}_{10}$ are unit vectors. From the definition of $\mathbf{u}(\boldsymbol{\tau})$, we have

$$\tau_{10} = -\frac{\langle \mathbf{u}(\boldsymbol{\tau}), *\mathbf{d_{10}} \rangle}{\langle \mathbf{d_{20}}, *\mathbf{d_{10}} \rangle}, \qquad \tau_{20} = \frac{\langle \mathbf{u}(\boldsymbol{\tau}), *\mathbf{d_{20}} \rangle}{\langle \mathbf{d_{10}}, *\mathbf{d_{20}} \rangle}.$$

14

By substituting eq. (30) in the above formulas, we obtain the following trigonometric parametrization of E:

$$\tau_{10}(\gamma) = -\frac{*(\mathbf{d_{10}} \wedge \mathbf{d_{20}})}{\langle \mathbf{d_{20}}, *\mathbf{d_{10}} \rangle} \left(\langle \tilde{\mathbf{d}}_{\mathbf{10}}, *\mathbf{d_{10}} \rangle \cos\gamma + \langle *\tilde{\mathbf{d}}_{\mathbf{10}}, *\mathbf{d_{10}} \rangle \sin\gamma \right),$$

$$\tau_{20}(\gamma) = \frac{*(\mathbf{d_{10}} \wedge \mathbf{d_{20}})}{\langle \mathbf{d_{10}}, *\mathbf{d_{20}} \rangle} \left(\langle \tilde{\mathbf{d}}_{\mathbf{10}}, *\mathbf{d_{20}} \rangle \cos\gamma + \langle *\tilde{\mathbf{d}}_{\mathbf{10}}, *\mathbf{d_{20}} \rangle \sin\gamma \right).$$

In the Euclidean plane, the identities $\langle *\mathbf{u}, *\mathbf{v} \rangle = \langle \mathbf{u}, \mathbf{v} \rangle$ and $\langle \mathbf{u}, *\mathbf{v} \rangle = *(\mathbf{u} \wedge \mathbf{v})$ hold for any $\mathbf{u}, \mathbf{v} \in \mathbb{R}^2$ (see Appendix A of [15]), therefore

$$\tau_{10}(\gamma) = d_{10} \sin\gamma$$

and

$$\tau_{20}(\gamma) = *(\tilde{\mathbf{d}}_{\mathbf{10}} \wedge \mathbf{d_{20}}) \cos\gamma + \langle \tilde{\mathbf{d}}_{\mathbf{10}}, \mathbf{d_{20}} \rangle \sin\gamma = d_{20}(\sin\varphi_0 \cos\gamma + \cos\varphi_0 \sin\gamma) = d_{20} \sin(\gamma + \varphi_0),$$

where in the second equality we used the assumption $*(\mathbf{d_{10}} \wedge \mathbf{d_{20}}) > 0$. $\qquad\square$

By substituting the above parametrization of E into $\|\hat{\boldsymbol{\tau}} - \boldsymbol{\tau}\|_{\boldsymbol{\Sigma_2}}^2$ and differentiating with respect to γ, we obtain the following trigonometric equation in $\gamma \in [0, 2\pi)$:

$$\langle \hat{\boldsymbol{\tau}} - \boldsymbol{\tau}(\gamma), (d_{10}\cos\gamma, d_{20}\cos(\gamma + \varphi_0)) \rangle_{\boldsymbol{\Sigma_2}} = 0. \tag{31}$$

For example, in the simplest case with $\boldsymbol{\Sigma_2} = \sigma^2 \mathbf{I}$, the equation is

$$d_{10}\cos\left(\tilde{\gamma} - \frac{\varphi_0}{2}\right)\left(\hat{\tau}_{10} - d_{10}\sin\left(\tilde{\gamma} - \frac{\varphi_0}{2}\right)\right) + d_{20}\cos\left(\tilde{\gamma} + \frac{\varphi_0}{2}\right)\left(\hat{\tau}_{20} - d_{20}\sin\left(\tilde{\gamma} + \frac{\varphi_0}{2}\right)\right) = 0,$$

where we used the more symmetric variable $\tilde{\gamma} = \gamma + \frac{\varphi_0}{2} \in [0, 2\pi)$. For any fixed setting of the sensors and the matrix $\boldsymbol{\Sigma_2}$, and for any TDOA measurements $\hat{\boldsymbol{\tau}} \in \mathbb{R}^2$, solutions $\bar{\gamma}_i$, $i = 1, \ldots, k$ of Equation (31) can be obtained through standard numerical algorithms (e.g. bisection or Newton–Raphson methods). Then, the relative orthogonal projections of $\hat{\boldsymbol{\tau}}$ on E are $\mathcal{P}_E^i(\hat{\boldsymbol{\tau}}; \boldsymbol{\Sigma_2}) = \boldsymbol{\tau}(\bar{\gamma}_i)$, $i = 1, \ldots, k$.

Irrespective of the chosen resolution method, for any projection we have to finally check if $\mathcal{P}_E^i(\hat{\boldsymbol{\tau}}; \boldsymbol{\Sigma_2})$ lies on the right arcs of ellipse for the given model. In particular, if we are considering model M, then we require $\mathcal{P}_E^i(\hat{\boldsymbol{\tau}}; \boldsymbol{\Sigma_2}) \in \partial U \cap E$, $i = 1, \ldots, k$. We showed in [15] that

$$\partial(U_0 \cup U_1 \cup U_2) \cap E \setminus \{T_0^{\pm}, T_1^{\pm}, T_2^{\pm}\} = C^+ \cap E \tag{32}$$

(see Figure 6). Since the set $\partial U \cap E$ is the complement in E of eq. (32), we have

$$\partial U \cap E = (C^- \cup C) \cap E. \tag{33}$$

By definition, $\mathcal{P}_E^i(\hat{\boldsymbol{\tau}}; \boldsymbol{\Sigma_2}) \in E$, $i = 1, \ldots, k$, thus $\mathcal{P}_E^i(\hat{\boldsymbol{\tau}}; \boldsymbol{\Sigma_2}) \in \partial U \cap E$ if, and only if, $b(\mathcal{P}_E^i(\hat{\boldsymbol{\tau}}; \boldsymbol{\Sigma_2})) \leq 0$. On the other hand, if we are considering the models M_j, $j = 0, 1, 2$, then we have to check if $\mathcal{P}_E^i(\hat{\boldsymbol{\tau}}; \boldsymbol{\Sigma_2}) \in \partial U_j \cap E$, $i = 1, \ldots, k$. This holds if and only if inequality $l_j(\mathcal{P}_E^i(\hat{\boldsymbol{\tau}}; \boldsymbol{\Sigma_2})) \geq 0$ is satisfied.

We conclude this subsection by discussing on the number k of solutions of system (29). For the case $\boldsymbol{\Sigma_2} = \sigma^2 \boldsymbol{I}$, this problem is known in the algebraic geometry literature (see [34, 50]) as the computation of the Euclidean distance degree of a variety (the ellipse E in the present case). We remark that the knowledge of k is crucial for the correct functioning of any numerical algorithm used for solving system (29).

Definition 7. *The Mahalanobis distance degree (MDdegree) of the ellipse E is the number of complex stationary points of the Lagrangian $\Lambda(\boldsymbol{\tau}, \nu; \hat{\boldsymbol{\tau}}; \boldsymbol{\Sigma_2})$ for a general $\hat{\boldsymbol{\tau}} \in \mathbb{C}^2$. The real Mahalanobis Degree (rMD) of E is the integer valued function $\kappa_{\boldsymbol{\Sigma_2}} : \mathbb{R}^2 \to \mathbb{N}$ that for any $\hat{\boldsymbol{\tau}} \in \mathbb{R}^2$ gives the number of distinct real stationary points of $\Lambda(\boldsymbol{\tau}, \nu; \hat{\boldsymbol{\tau}}; \boldsymbol{\Sigma_2})$. Finally, the Mahalanobis degree discriminant (MDdiscriminant) of E is the locus $\mathcal{E}_{\boldsymbol{\Sigma_2}} \subset \mathbb{C}^2$ of points $\hat{\boldsymbol{\tau}} \in \mathbb{R}^2$ such that $\Lambda(\boldsymbol{\tau}, \nu; \hat{\boldsymbol{\tau}}; \boldsymbol{\Sigma_2})$ has at least two coinciding stationary points.*
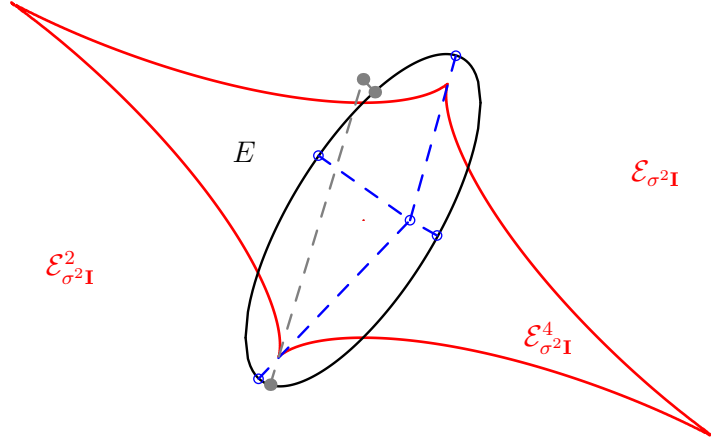
Figure 7: The MDdiscriminant $\mathcal{E}_{\boldsymbol{\Sigma_2}}$ of the ellipse E when $\boldsymbol{\Sigma_2} = \sigma^2 \mathbf{I}$ and the regions $\mathcal{E}^2_{\boldsymbol{\Sigma_2}}, \mathcal{E}^4_{\boldsymbol{\Sigma_2}}$, for the configuration of the receiver $\mathbf{m_0} = (0,0)^T$, $\mathbf{m_1} = (2,0)^T$ and $\mathbf{m_2} = (2,2)^T$. If $\hat{\boldsymbol{\tau}} \in \mathcal{E}^4_{\boldsymbol{\Sigma_2}}$ there are 4 projections on E, if $\hat{\boldsymbol{\tau}} \in \mathcal{E}^2_{\boldsymbol{\Sigma_2}}$ there are 2 projections and finally for $\hat{\boldsymbol{\tau}} \in \mathcal{E}_{\boldsymbol{\Sigma_2}}$ there are 3 distinct projections.

The interested reader can find in [34, 50] the definition of the distance degree and discriminant for any given variety and the proofs of the following results. As it is implicit in its definition, MDdegree does not depend on $\hat{\boldsymbol{\tau}}$ and $\boldsymbol{\Sigma_2}$ and for every ellipse it is equal to 4. The MDdiscriminant $\mathcal{E}_{\boldsymbol{\Sigma_2}}$ is an astroid, i.e. an algebraic singular curve of degree six whose real part is of the type drawn in Figure 7.

Although the shape of the astroid depends on the covariance matrix, its topological properties are invariant and in particular $\mathcal{E}_{\boldsymbol{\Sigma_2}}$ subdivides the τ–plane into two connected and disjoint open regions: the exterior and the interior of $\mathcal{E}_{\boldsymbol{\Sigma_2}}$, that we name $\mathcal{E}^2_{\boldsymbol{\Sigma_2}}$ and $\mathcal{E}^4_{\boldsymbol{\Sigma_2}}$, respectively. The function $\kappa_{\boldsymbol{\Sigma_2}}$ is constant on each of these regions and in particular we have:

$$\kappa_{\boldsymbol{\Sigma_2}}(\hat{\boldsymbol{\tau}}) = \begin{cases} 2 & \text{if, and only if,} \quad \hat{\boldsymbol{\tau}} \in \mathcal{E}^2_{\boldsymbol{\Sigma_2}} \\ 3 & \text{if, and only if,} \quad \hat{\boldsymbol{\tau}} \in \mathcal{E}_{\boldsymbol{\Sigma_2}} \\ 4 & \text{if, and only if,} \quad \hat{\boldsymbol{\tau}} \in \mathcal{E}^4_{\boldsymbol{\Sigma_2}} \end{cases} . \tag{34}$$

Notice that $\kappa_{\boldsymbol{\Sigma_2}}(\hat{\boldsymbol{\tau}})$ is exactly the number k of orthogonal projections $\mathcal{P}^i_E(\hat{\boldsymbol{\tau}}; \boldsymbol{\Sigma_2})$ of the point $\hat{\boldsymbol{\tau}} \in \mathbb{R}^2$ on the ellipse E. In Appendix A we include the source code (written in Singular [51]) for computing the Cartesian equation $F_{\boldsymbol{\Sigma_2}}(\boldsymbol{\tau}) = 0$ of $\mathcal{E}_{\boldsymbol{\Sigma_2}}$, once the sensors positions and the covariance matrix have been set. As an example, the polynomial defining the curve $\mathcal{E}_{\sigma^2 I}$ in Figure 7 is:

$$\begin{aligned} F_{\sigma^2 I}(\boldsymbol{\tau}) &= \tau_1^6 + 6\tau_1^5\tau_2 + 18\tau_1^4\tau_2^2 + 32\tau_1^3\tau_2^3 + 36\tau_1^2\tau_2^4 + 24\tau_1\tau_2^5 + 8\tau_2^6 + 48\tau_1^4 - 24\tau_1^3\tau_2 \\ &\quad -588\tau_1^2\tau_2^2 - 696\tau_1\tau_2^3 - 132\tau_2^4 + 1200\tau_1^2 + 2400\tau_1\tau_2 + 2400\tau_2^2 - 8000. \end{aligned}$$

As $\mathbf{0} = (0,0)^T \in \mathcal{E}^4_{\boldsymbol{\Sigma_2}}$, a point $\hat{\boldsymbol{\tau}} \in \mathbb{R}^2$ lies on $\mathcal{E}^4_{\boldsymbol{\Sigma_2}}$ (respectively $\mathcal{E}^2_{\boldsymbol{\Sigma_2}}$) if, and only if, $F_{\boldsymbol{\Sigma_2}}(\hat{\boldsymbol{\tau}})F_{\boldsymbol{\Sigma_2}}(\mathbf{0}) > 0$ (respectively $F_{\boldsymbol{\Sigma_2}}(\hat{\boldsymbol{\tau}})F_{\boldsymbol{\Sigma_2}}(\mathbf{0}) < 0$).

5. Asymptotic statistical inference

A crucial point in parametric statistics is the evaluation of the accuracy of parameter estimation procedures. The precise description of the parametric models M, M_0, M_1, M_2 given in Section 3 allows us to use the tools of Information Geometry [22] for analyzing this aspect of TDOA–based localization. In Section 4 we laid down the basis for the solution of MLE, that is the optimal estimation from the statistical point of view. Now we focus on the analysis of MLE efficiency. In Section 6 we will explicitly implement the MLE and validate our theoretical analysis.

Notice that the analysis proposed in this manuscript is inherently local, based on the differential geometry properties of the restricted models. In particular, this means that here we do not take into account the ambiguities in the localization, which we described in Section 2. What we do is to study an ideal situation, where we know the region $\Omega, \Omega_1, \Omega_2, \Omega_3$ where the source lies, and therefore we know which TDOA model to consider. At the end of Section 6, we will go back to the more realistic scenario in which we have no a-priori knowledge on the source position.

We finally remark that the analytic evaluation of the accuracy of source localization is not a novel idea per se. See [24, 25] for other examples that do not rely on Information Geometry. This manuscript, however, goes further in that investigation as it proposes in Section 5.2 a study on the reliability of the asymptotic analysis.

5.1. Asymptotic mean square error and bias of MLE

From Theorem 5, we know that each model M, M_0, M_1, M_2 is a $(2, 2)$ curved exponential family. As $\mathbf{\Sigma_2}$ is known, we only have to specify the parameters $\boldsymbol{\theta}(\mathbf{x}) = \boldsymbol{\tau_2}(\mathbf{x})$. It is well-known that for any statistical manifold, there exists a natural Riemannian metric, the so called *Fisher metric*. If we use $E_{\mathbf{x}}[\cdot]$ to denote the expectation value with respect to the distribution $p(\hat{\boldsymbol{\tau}}; \boldsymbol{\theta}(\mathbf{x}))$, then at any point $\boldsymbol{\theta}(\mathbf{x})$ the metric is given by the Fisher information matrix

$$\mathbf{G}(\mathbf{x}) = E_{\mathbf{x}}[\nabla_{\mathbf{x}} \ell(\hat{\boldsymbol{\tau}}; \boldsymbol{\theta}(\mathbf{x}))^T \, \nabla_{\mathbf{x}} \ell(\hat{\boldsymbol{\tau}}; \boldsymbol{\theta}(\mathbf{x}))] = \int_{\mathbb{R}^2} \nabla_{\mathbf{x}} \ell(\hat{\boldsymbol{\tau}}; \boldsymbol{\theta}(\mathbf{x}))^T \, \nabla_{\mathbf{x}} \ell(\hat{\boldsymbol{\tau}}; \boldsymbol{\theta}(\mathbf{x})) \, p(\hat{\boldsymbol{\tau}}; \boldsymbol{\theta}(\mathbf{x})) \mathrm{d}\hat{\boldsymbol{\tau}},$$

where $\nabla_{\mathbf{x}} \ell(\hat{\boldsymbol{\tau}}; \boldsymbol{\theta}(\mathbf{x})) = (\partial_x \ell(\hat{\boldsymbol{\tau}}; \boldsymbol{\theta}(\mathbf{x})), \partial_y \ell(\hat{\boldsymbol{\tau}}; \boldsymbol{\theta}(\mathbf{x})))$. In the integral it appears the function

$$\ell(\hat{\boldsymbol{\tau}}; \boldsymbol{\theta}(\mathbf{x})) = \ln(p(\hat{\boldsymbol{\tau}}; \boldsymbol{\theta}(\mathbf{x}))) = C(\hat{\boldsymbol{\tau}}) + \sum_{i=1}^{n} \theta_i(\mathbf{x}) F_i(\hat{\boldsymbol{\tau}}) - \psi(\boldsymbol{\theta}(\mathbf{x})),$$

where

$$C(\hat{\boldsymbol{\tau}}) = -\frac{1}{2} \|\hat{\boldsymbol{\tau}}\|_{\mathbf{\Sigma_2}}^2, \quad F_i(\hat{\boldsymbol{\tau}}) = (\mathbf{\Sigma_2}^{-1}\hat{\boldsymbol{\tau}})_i, \quad \psi(\boldsymbol{\theta}(\mathbf{x})) = \frac{1}{2} \|\boldsymbol{\theta}(\mathbf{x})\|_{\mathbf{\Sigma_2}}^2 + \log \sqrt{(2\pi)^n |\mathbf{\Sigma_2}|}.$$

In order to explicitly obtain the Fisher matrix, we compute the Jacobian matrix of $\boldsymbol{\theta}(\mathbf{x})$:

$$\mathbf{J}(\boldsymbol{\theta}(\mathbf{x})) = \begin{pmatrix} \tilde{\mathbf{d}}_1(\mathbf{x}) - \tilde{\mathbf{d}}_0(\mathbf{x}) \\ \tilde{\mathbf{d}}_2(\mathbf{x}) - \tilde{\mathbf{d}}_0(\mathbf{x}) \end{pmatrix}.$$

After some straightforward computations we obtain

$$\mathbf{G}(\mathbf{x}) = \mathbf{J}(\boldsymbol{\theta}(\mathbf{x}))^T \mathbf{\Sigma_2}^{-1} \mathbf{J}(\boldsymbol{\theta}(\mathbf{x})).$$

Furthermore, the Hessian matrices of the components of $\boldsymbol{\theta}(\mathbf{x})$ with respect to the parameters $\mathbf{x}$ are:

$$\mathbf{Hs}(\theta_i(\mathbf{x})) = \begin{pmatrix} \frac{\langle \tilde{\mathbf{d}}_i, \mathbf{e}_2 \rangle^2}{d_i} & -\frac{\langle \tilde{\mathbf{d}}_i, \mathbf{e}_1 \rangle \langle \tilde{\mathbf{d}}_i, \mathbf{e}_2 \rangle}{d_i} \\ -\frac{\langle \tilde{\mathbf{d}}_i, \mathbf{e}_1 \rangle \langle \tilde{\mathbf{d}}_i, \mathbf{e}_2 \rangle}{d_i} & \frac{\langle \tilde{\mathbf{d}}_i, \mathbf{e}_1 \rangle^2}{d_i} \end{pmatrix} - \begin{pmatrix} \frac{\langle \tilde{\mathbf{d}}_0, \mathbf{e}_2 \rangle^2}{d_0} & -\frac{\langle \tilde{\mathbf{d}}_0, \mathbf{e}_1 \rangle \langle \tilde{\mathbf{d}}_0, \mathbf{e}_2 \rangle}{d_0} \\ -\frac{\langle \tilde{\mathbf{d}}_0, \mathbf{e}_1 \rangle \langle \tilde{\mathbf{d}}_0, \mathbf{e}_2 \rangle}{d_0} & \frac{\langle \tilde{\mathbf{d}}_0, \mathbf{e}_1 \rangle^2}{d_0} \end{pmatrix},$$

for $i = 1, 2$. Now, we can state the main result of this section. As we saw in Section 4.1, for any set of measurements $\hat{\boldsymbol{\tau}}$ and for each model we have an MLE estimate $\bar{\boldsymbol{\tau}}(\hat{\boldsymbol{\tau}}; \mathbf{\Sigma_2})$ and a corresponding source position $\bar{\mathbf{x}}(\hat{\boldsymbol{\tau}}; \mathbf{\Sigma_2}) = \boldsymbol{\tau_2}^{-1}(\bar{\boldsymbol{\tau}}(\hat{\boldsymbol{\tau}}; \mathbf{\Sigma_2}))$.

Proposition 8. *Given a source at* $\mathbf{x}$, *the (local) asymptotic mean square error of* $\bar{\mathbf{x}}(\hat{\boldsymbol{\tau}}; \mathbf{\Sigma_2})$ *is equal to*

$$E_{\mathbf{x}}[(\bar{\mathbf{x}}(\hat{\boldsymbol{\tau}}; \mathbf{\Sigma_2}) - \mathbf{x})^T (\bar{\mathbf{x}}(\hat{\boldsymbol{\tau}}; \mathbf{\Sigma_2}) - \mathbf{x})] = \mathbf{G}(\mathbf{x})^{-1}. \tag{35}$$

The (local) first order bias of $\bar{\mathbf{x}}(\hat{\boldsymbol{\tau}}; \mathbf{\Sigma_2})$ *is*

$$E_{\mathbf{x}}[\bar{\mathbf{x}}(\hat{\boldsymbol{\tau}}; \mathbf{\Sigma_2}) - \mathbf{x}] = -\frac{1}{2} \mathbf{b}(\mathbf{x}), \tag{36}$$

where

$$\mathbf{b}(\mathbf{x}) = \left(\mathrm{Tr}(\mathbf{Hs}(\theta_1(\mathbf{x}))\mathbf{G}(\mathbf{x})^{-1}), \mathrm{Tr}(\mathbf{Hs}(\theta_2(\mathbf{x}))\mathbf{G}(\mathbf{x})^{-1}) \right) \cdot (\mathbf{J}(\boldsymbol{\theta}(\mathbf{x}))^{-1})^T. \tag{37}$$

17

Proof. The formula for the asymptotic mean square error of a consistent estimator is given in Theorem 4.3 of [22]. Since MLE is consistent and asymptotically efficient, such formula reduces to Equation (35).[3] Moreover, by considering the higher order asymptotic theory, one can compute the expected value in Equation (36). It is just a matter of computation to verify that Equation (37) is equivalent to formula 4.42 in [22]. $\square$

In the case $\boldsymbol{\Sigma_2} = \sigma^2 \mathbf{I}$, Equation (35) reduces to:

$$\mathbf{G}(\mathbf{x})^{-1} = \frac{\sigma^2}{|J(\boldsymbol{\eta}(\mathbf{x}))|^2} \sum_{i=1}^{2} \begin{pmatrix} g_{i,22} & -g_{i,12} \\ -g_{i,12} & g_{i,11} \end{pmatrix},$$

where $g_{i,jk} = \langle \tilde{\mathbf{d}}_{\mathbf{i}} - \tilde{\mathbf{d}}_{\mathbf{0}}, \mathbf{e}_{\mathbf{j}} \rangle \langle \tilde{\mathbf{d}}_{\mathbf{i}} - \tilde{\mathbf{d}}_{\mathbf{0}}, \mathbf{e}_{\mathbf{k}} \rangle$, $i, j, k = 0, 1, 2$.

The a priori knowledge of the bias is very interesting from the point of view of applications, because it allows us to define the bias-corrected MLE as

$$\bar{\mathbf{x}}_{bc}(\hat{\boldsymbol{\tau}}; \boldsymbol{\Sigma_2}) = \bar{\mathbf{x}}(\hat{\boldsymbol{\tau}}; \boldsymbol{\Sigma_2}) + \frac{1}{2}\mathbf{b}(\mathbf{x}). \tag{38}$$

However, an exact compensation of the bias involves the knowledge of the true source location $\mathbf{x}$, which is obviously unknown in real context. At best, one can compute the bias at the estimated source location, and so the bias-compensated estimate becomes

$$\bar{\mathbf{x}}_{bc}(\hat{\boldsymbol{\tau}}; \boldsymbol{\Sigma_2}) = \bar{\mathbf{x}}(\hat{\boldsymbol{\tau}}; \boldsymbol{\Sigma_2}) + \frac{1}{2}\mathbf{b}(\bar{\mathbf{x}}(\hat{\boldsymbol{\tau}}; \boldsymbol{\Sigma_2})). \tag{39}$$

An inexact knowledge of the source location introduces an error in the bias prediction. With some preliminary experiments we tested that Equation (39) improves the estimate of the distance of the source from the reference sensor, while the variance of the direction of arrival increases. This suggests that an improved accuracy could be achieved by using the estimation of the distance and of the angle coming from bias-corrected and non-corrected estimations, respectively. However, we leave a deeper analysis of such a problem for future developments.

5.2. Assessment of the asymptotic analysis

The asymptotic error analysis described in the previous Section gives a faithful evaluation of the error relative to the source position only under certain conditions. In general, the asymptotic error analysis works where the curvature of the statistical manifold is not too high, as explained in Section 4.5 of [22]. In our case, for each one of the four models M, M_0, M_1, M_2, it works well if we keep away from their boundaries.

In this Section we propose a method for evaluating the reliability of the asymptotic analysis. The starting observation is that the asymptotic error analysis is essentially based on taking the first non-trivial orders in the Taylor expansions of the expectation values given in (35) and (36), respectively. A first possible approach is to consider the rest of such approximations by taking the Lagrange remainders of the respective Taylor polynomials. However, preliminary tests indicate that, in doing so, we typically overestimate the errors caused by the low-order approximations.

More realistically, we can estimate the error in the asymptotic approximation by computing the next order in the series expansions of (35) and (36). The key identity is

$$E_{\mathbf{x}}[f(\hat{\boldsymbol{\tau}})] = \int_{\mathbb{R}^2} f(\hat{\boldsymbol{\tau}})\, p(\hat{\boldsymbol{\tau}}; \boldsymbol{\theta}(\mathbf{x}))\, \mathbf{d}\hat{\boldsymbol{\tau}} = \exp\left[\frac{1}{2}\nabla \boldsymbol{\Sigma_2} \nabla^T\right] f(\hat{\boldsymbol{\tau}})\bigg|_{\hat{\boldsymbol{\tau}} = \boldsymbol{\theta}(\mathbf{x})}$$

where the exponential differential operator corresponds to the power series

$$\exp\left[\frac{1}{2}\nabla \boldsymbol{\Sigma_2} \nabla^T\right] = \sum_{n=0}^{\infty} \frac{1}{2^n n!} \left(\sum_{i,j=1}^{2} \boldsymbol{\Sigma_2}_{ij} \frac{\partial}{\partial \hat{\tau}_i} \frac{\partial}{\partial \hat{\tau}_j}\right)^n.$$

---

[3] Actually, this way we obtain the Cramer–Rao lower bound.

For the sake of simplicity, here we focus on the analysis of Equation (35) under the assumption $\mathbf{\Sigma_2} = \sigma^2 \mathbf{I}$. We have

$$f(\hat{\boldsymbol{\tau}}) = \left((\bar{\mathbf{x}}(\hat{\boldsymbol{\tau}};\mathbf{\Sigma_2}) - \mathbf{x})^T (\bar{\mathbf{x}}(\hat{\boldsymbol{\tau}};\mathbf{\Sigma_2}) - \mathbf{x})\right)_{ij}, \quad i,j = 1,2.$$

If $\hat{\boldsymbol{\tau}}$ lies on the interior of a given model, the MLE is simply the inverse map, i.e. $\bar{\mathbf{x}}(\hat{\boldsymbol{\tau}};\mathbf{\Sigma_2}) = \boldsymbol{\tau_2}^{-1}(\hat{\boldsymbol{\tau}})$. Therefore, it is a matter of computation to obtain the first order correction $\mathbf{\Delta}(\mathbf{x})$ to the expectation value (35). In order to simplify the explanation, in the formula we use the following multi-index notation:

$$D_i^{pq} = \left(\left.\frac{\partial^{p+q}}{\partial \hat{\tau}_1^p \, \partial \hat{\tau}_2^q} \, \boldsymbol{\tau_2}^{-1}(\hat{\boldsymbol{\tau}})\right|_{\hat{\boldsymbol{\tau}}=\boldsymbol{\theta}(\mathbf{x})}\right)_i, \quad i = 1,2, \;\; p,q = 0,1,2.$$

This way, we arrive to

$$\mathbf{\Delta}(\mathbf{x})_{ij} = \left(E_{\mathbf{x}}[(\bar{\mathbf{x}}(\hat{\boldsymbol{\tau}};\mathbf{\Sigma_2}) - \mathbf{x})^T (\bar{\mathbf{x}}(\hat{\boldsymbol{\tau}};\mathbf{\Sigma_2}) - \mathbf{x})] - \mathbf{G}(\mathbf{x})^{-1}\right)_{ij} =$$

$$\frac{\sigma^4}{4} \left(3 \left(D_i^{20} D_j^{20} + D_i^{02} D_j^{02}\right) + D_i^{20} D_j^{02} + D_i^{02} D_j^{20} + 4 D_i^{11} D_j^{11} + \right.$$

$$\left. +2 D_i^{10} \left(D_j^{30} + D_j^{12}\right) + 2 D_i^{01} \left(D_j^{03} + D_j^{21}\right) + 2 D_j^{10} \left(D_i^{30} + D_i^{12}\right) + 2 D_j^{10} \left(D_i^{30} + D_i^{21}\right)\right) + o(\sigma^5).$$

In Section 6 we will validate this formula through simulations and we will suggest how it can be used for the evaluation of the accuracy of the asymptotic error analysis given in Proposition 8.

6. MLE algorithms implementation and validation

This Section implements the MLE localization technique and the asymptotic statistical analysis in Sections 4 and 5, respectively. In particular, we will validate them through a set of simulations. Finally, we conclude by offering some comments for the reader who might be interested in adopting the described algorithm in a real scenario.

6.1. The solutions of the MLE

As discussed in Section 4, we have a different MLE for models M and M_i, $i = 1,2,3$. In all these cases we are interested in computing the estimate $\bar{\mathbf{x}}(\hat{\boldsymbol{\tau}};\mathbf{\Sigma_2})$ from the data vector $\hat{\boldsymbol{\tau}}$. We begin with the model M, therefore we assume that $\mathbf{x} \in \Omega$.

Algorithm 1 MLE algorithm for model M

Input: TDOA measurements $\hat{\boldsymbol{\tau}}$, covariance matrix $\mathbf{\Sigma_2}$
Output: $\bar{\mathbf{x}}(\hat{\boldsymbol{\tau}};\mathbf{\Sigma_2})$
1: Check if $\hat{\boldsymbol{\tau}}$ lies in U by verifying the (strict) inequalities (5) and (23). If so $\bar{\boldsymbol{\tau}}(\hat{\boldsymbol{\tau}};\mathbf{\Sigma_2}) = \hat{\boldsymbol{\tau}}$ and go to Line 5.
2: Compute the orthogonal projections $\mathcal{P}_i^{\pm}(\hat{\boldsymbol{\tau}};\mathbf{\Sigma_2})$, $i = 0,1,2$, by using formulas (28) and $\mathcal{P}_E^j(\hat{\boldsymbol{\tau}};\mathbf{\Sigma_2})$, $j = 1,\ldots,k$, by solving system (29).
3: Evaluate which of the projections lie on ∂U. For $\mathcal{P}_i^{\pm}(\hat{\boldsymbol{\tau}};\mathbf{\Sigma_2})$, $i = 0,1,2$, one hase to check inequalities (5) and $l_i(\mathcal{P}_i^{\pm}(\hat{\boldsymbol{\tau}};\mathbf{\Sigma_2})) \geq 0$. For $\mathcal{P}_E^j(\hat{\boldsymbol{\tau}};\mathbf{\Sigma_2})$, $j = 1,\ldots,k$, one has to verify $b(\mathcal{P}_E^j(\hat{\boldsymbol{\tau}};\mathbf{\Sigma_2})) \leq 0$.
4: For every projection on ∂U and for each vertex R^i, $i = 0,1,2$, compute the Mahalanobis distance from $\hat{\boldsymbol{\tau}}$. The MLE solution $\bar{\boldsymbol{\tau}}(\hat{\boldsymbol{\tau}};\mathbf{\Sigma_2})$ corresponds to the point where such distance is minimum.
5: The estimated source position is $\bar{\mathbf{x}}(\hat{\boldsymbol{\tau}};\mathbf{\Sigma_2}) = \mathbf{x}_+(\bar{\boldsymbol{\tau}}(\hat{\boldsymbol{\tau}};\mathbf{\Sigma_2}))$.

We must pay attention to the interpretation of the results regarding the source position. Indeed, by taking the closest point to $\hat{\boldsymbol{\tau}}$ on ∂U, we are actually considering the *compactification* of the model M. We have the following cases.

a) If $\bar{\boldsymbol{\tau}}(\hat{\boldsymbol{\tau}};\mathbf{\Sigma_2})$ is one of the $\mathcal{P}_i^{\pm}(\hat{\boldsymbol{\tau}};\mathbf{\Sigma_2})$, $i = 0,1,2$, then $\bar{\mathbf{x}}(\hat{\boldsymbol{\tau}};\mathbf{\Sigma_2})$ lies on the degeneracy locus D.

b) If $\bar{\boldsymbol{\tau}}(\hat{\boldsymbol{\tau}}; \boldsymbol{\Sigma_2})$ is one of the $\mathcal{P}_E^j(\hat{\boldsymbol{\tau}}; \boldsymbol{\Sigma_2})$, $j = 1, \ldots, k$, then we have to take the extension of the inverse map $\mathbf{x}_+(\boldsymbol{\tau})$ with value in the projective plane, because $\lambda_+(\boldsymbol{\tau})$ is not defined on $\partial U \cap E$. It follows that $\bar{\mathbf{x}}(\hat{\boldsymbol{\tau}}; \boldsymbol{\Sigma_2})$ is the ideal point with homogeneous coordinates $(\mathbf{v}(\mathcal{P}_E^j(\hat{\boldsymbol{\tau}}; \boldsymbol{\Sigma_2})) : 0) \in \mathbb{P}_\mathbb{R}^2$. In this case, the vector $\mathbf{v}(\mathcal{P}_E^j(\hat{\boldsymbol{\tau}}; \boldsymbol{\Sigma_2}))$ should be interpreted as the localization direction of a very far source, in a situation where even a very small noise on the TDOA measurements hinders to estimate the distance of the source from the sensors.

c) If $\bar{\boldsymbol{\tau}}(\hat{\boldsymbol{\tau}}; \boldsymbol{\Sigma_2}) = R^i$, then $\bar{\mathbf{x}}(\hat{\boldsymbol{\tau}}; \boldsymbol{\Sigma_2}) = \mathbf{m_i}$, $i = 0, 1, 2$.

A similar MLE algorithm can be defined for each model M_i, $i = 0, 1, 2$. In these cases, we are assuming that $\mathbf{x} \in \Omega_i$.

Algorithm 2 MLE algorithm for model M_i

Input: TDOA measurements $\hat{\boldsymbol{\tau}}$, covariance matrix $\boldsymbol{\Sigma_2}$
Output: $\bar{\mathbf{x}_i}(\hat{\boldsymbol{\tau}}; \boldsymbol{\Sigma_2})$
 1: Check if $\hat{\boldsymbol{\tau}}$ lies on U_i by verifying the (strict) inequalities (5) and (9). If so $\bar{\boldsymbol{\tau}}_i(\hat{\boldsymbol{\tau}}; \boldsymbol{\Sigma_2}) = \hat{\boldsymbol{\tau}}$ and go to Line 5.
 2: Compute the orthogonal projections $\mathcal{P}_i^\pm(\hat{\boldsymbol{\tau}}; \boldsymbol{\Sigma_2})$ by using formulas (28) and $\mathcal{P}_E^j(\hat{\boldsymbol{\tau}}; \boldsymbol{\Sigma_2})$, $j = 1, \ldots, k$, by solving system (29).
 3: Evaluate which of the projections lie on ∂U_i. For $\mathcal{P}_i^\pm(\hat{\boldsymbol{\tau}}; \boldsymbol{\Sigma_2})$ one has to check inequalities (5) and $l_i(\mathcal{P}_i^\pm(\hat{\boldsymbol{\tau}}; \boldsymbol{\Sigma_2})) \geq 0$. For $\mathcal{P}_E^j(\hat{\boldsymbol{\tau}}; \boldsymbol{\Sigma_2})$, $j = 1, \ldots, k$, one has to verify $l_i(\mathcal{P}_E^j(\hat{\boldsymbol{\tau}}; \boldsymbol{\Sigma_2})) \geq 0$.
 4: For every projection on ∂U_i and for the vertex R^i calculate the Mahalanobis distance from $\hat{\boldsymbol{\tau}}$. The MLE solution $\bar{\boldsymbol{\tau}}_i(\hat{\boldsymbol{\tau}}; \boldsymbol{\Sigma_2})$ is the point where such distance is minimum.
 5: The estimated source position is $\bar{\mathbf{x}_i}(\hat{\boldsymbol{\tau}}; \boldsymbol{\Sigma_2}) = \mathbf{x}_-(\bar{\boldsymbol{\tau}}_i(\hat{\boldsymbol{\tau}}; \boldsymbol{\Sigma_2}))$.

Similar remarks to those offered for the model M hold true in this case as well.

We recommend to be careful about the numerical stability of the solutions of the quadratic equation $a(\boldsymbol{\tau})\lambda_\pm(\boldsymbol{\tau})^2 + 2b(\boldsymbol{\tau})\lambda_\pm(\boldsymbol{\tau}) + c(\boldsymbol{\tau}) = 0$ contained in Section 2. This can become an issue especially when $\boldsymbol{\tau}$ is close to the ellipse E and so $a(\boldsymbol{\tau}) \simeq 0$. In this case the quadratic equation is ill conditioned and so formula (13) should not be used. See for example [52] as a reference book on this topic. Finally, let us briefly comment the computational complexity of the algorithms. Every operation involved in both Algorithms 1 and 2 requires a single iteration for each measurement, except for the projection of the measured TDOAs on the ellipse. As suggested in Section 4, this computation can be implemented using iterative techniques such as Newton-Raphson method. However, it is important to notice that each step of the iterative solution requires only 6 multiplications and 7 sums. Furthermore, the number of iterations does not depend on the search space of the source location. Therefore, we believe that the proposed localization technique is particularly suitable for applications that require a frequent estimation of the source location at a reduced computational burden, such as camera steering for video-conferencing and audio-surveillance.

6.2. Simulative results and comparison with asymptotical statistical inference

In this subsection we show the experimental results about source localization based on Algorithms 1 and 2. We evaluate them through asymptotic analysis and Monte Carlo simulations.

6.2.1. Setup

The sensors are deployed as in Figure 4, i.e. $\mathbf{m}_0 = (0, 0)^T$, $\mathbf{m}_1 = (2, 0)^T$ and $\mathbf{m}_2 = (2, 2)^T$, and the reference sensor is $\mathbf{m}_0$. The covariance matrix is $\boldsymbol{\Sigma_2} = \sigma^2 \mathbf{I}$, where $\sigma = 0.005$ m. Notice that both root mean square error and bias are proportional to the noise variance, and therefore results do not lose generality due to the choice of a specific value of σ. Sources are placed on a regular grid centered around the center of gravity of the sensors. In particular, the x and y coordinates range from -2.67 m to 5.33 m and from -3.33 m to 5.33 m, respectively, resulting in a total number of 4225 test source locations. For each source

location $\mathbf{x}$ in the lattice, we simulate $N = 500$ noisy TDOA measurements $\hat{\boldsymbol{\tau}}_j(\mathbf{x}) = \boldsymbol{\tau_2}(\mathbf{x}) + \boldsymbol{\epsilon_{2,j}}$, $1 \leq j \leq N$. Then, we compute the sample estimates of the mean square error matrix and the bias:

$$\widehat{\mathbf{M}}(\mathbf{x}) = \sum_{j=1}^{N} \frac{\left(\bar{\mathbf{x}}(\hat{\boldsymbol{\tau}}_j(\mathbf{x}); \boldsymbol{\Sigma_2}) - \mathbf{x}\right)\left(\bar{\mathbf{x}}(\hat{\boldsymbol{\tau}}_j(\mathbf{x}); \boldsymbol{\Sigma_2}) - \mathbf{x}\right)^T}{N} \quad \text{and} \quad \widehat{\mathbf{B}}(\mathbf{x}) = \sum_{j=1}^{N} \frac{\bar{\mathbf{x}}(\hat{\boldsymbol{\tau}}_j(\mathbf{x}); \boldsymbol{\Sigma_2}) - \mathbf{x}}{N}.$$

We use Algorithms 1 and 2 according to the position of the true source $\mathbf{x}$. In order to discriminate the distance and angular error components on the source location, the projections of $\widehat{\mathbf{M}}(\mathbf{x})$ and $\widehat{\mathbf{B}}(\mathbf{x})$ on the eigenvectors of the matrix $\mathbf{G}^{-1}(\mathbf{x})$ are computed. Indeed, for sufficiently distant sources, the eigenvector related to the largest eigenvalue approximately coincides with the direction of the source, as seen from the array (in the following called radial direction). Due to the dynamic range of the error along the radial component, we adopt a logarithmic transformation of the component of the covariance matrix (predicted or estimated) along the radial direction.

6.2.2. Mean Square Error

Figure 8 shows the mean square error on localization predicted by $\mathbf{G}^{-1}(\mathbf{x})$ (first row) and the simulated one $\widehat{\mathbf{M}}(\mathbf{x})$ (second row), for the component along the radial direction (a) and the orthogonal one (b). It is important to notice that in the area enclosed by the microphones, both the radial and the angular error components do not exceed 0.01 m, thus confirming the validity of the MLE solution. If the sources is farther from the microphones, the error increases, but it is still reasonable at a distance of $2 - 3$ m. By comparing prediction and simulation results, we can notice that the asymptotic prediction is quite accurate over the considered region, except for the areas surrounding the degeneracy locus D, i.e. the half-lines $r_i^{\pm}$, $i = 0, 1, 2$ prolongations of the segments joining the sensor locations.
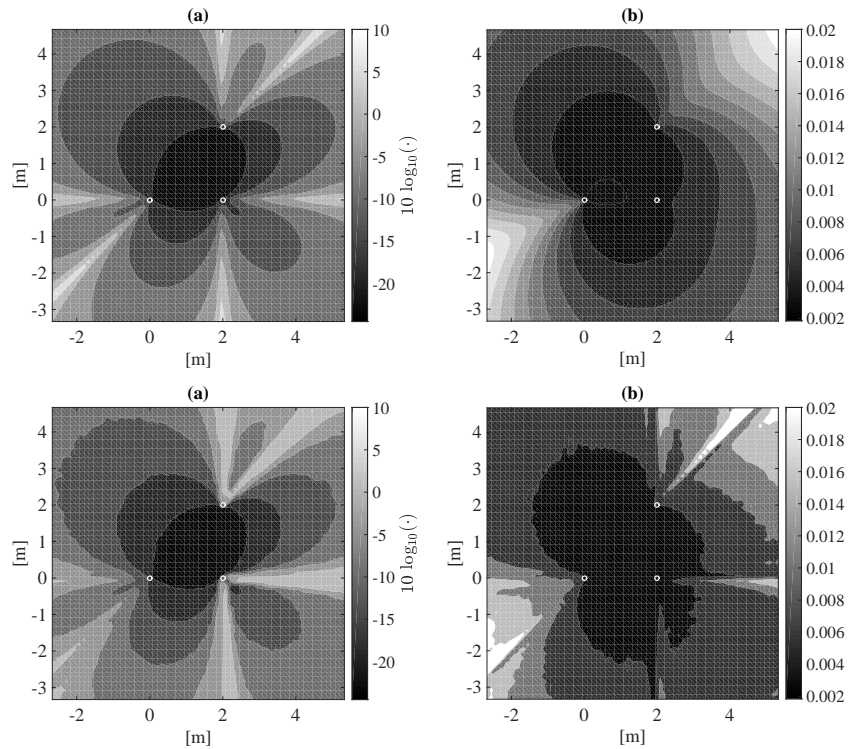

Figure 8: Projection of $\mathbf{G}^{-1}(\mathbf{x})$ (first row) and $\widehat{\mathbf{M}}(\mathbf{x})$ (second row) along the eigenvectors of $\mathbf{G}^{-1}(\mathbf{x})$. Projections along the eigenvectors related to the maximum (a) and minimum (b) eigenvalue of $\mathbf{G}^{-1}(\mathbf{x})$ are shown. Results are expressed on a logarithmic scale (a) and in meters (b).

With the aim of assessing the accuracy of the asymptotical estimate, in Figure 9 we compare the remainder $\boldsymbol{\Delta}(\mathbf{x})$ computed according to Section 5.2 and the difference $\widehat{\boldsymbol{\Delta}}(\mathbf{x}) = \widehat{M}(\mathbf{x}) - \mathbf{G}^{-1}(\mathbf{x})$ between simulated and predicted MSE. The solid lines are level curves of $\boldsymbol{\Delta}(\mathbf{x})$, while the colormap represents $\widehat{\boldsymbol{\Delta}}(\mathbf{x})$. We can observe a pretty good match between the two. Such comparison suggests that we can use $\boldsymbol{\Delta}(\mathbf{x})$ as a reliability certificate for the asymptotic prediction of MSE given by $\mathbf{G}^{-1}(\mathbf{x})$. For example, one could define the trusted region of $\mathbf{G}^{-1}(\mathbf{x})$ as the one where $\boldsymbol{\Delta}(\mathbf{x})$ takes value below a suitable threshold.

The availability of a method to predict the MSE is important in applications where different accuracy is required in different regions. However, a quantitative estimate of $\boldsymbol{\Delta}(\mathbf{x}) - \widehat{\boldsymbol{\Delta}}(\mathbf{x})$ in the most general case is beyond the scope of the manuscript and needs further investigation.
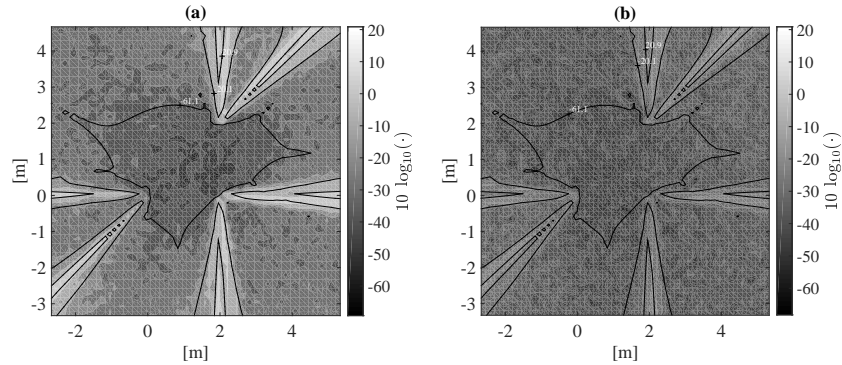

Figure 9: Superposition of the contour lines of $\boldsymbol{\Delta}(\mathbf{x})$ (solid lines), and $\widehat{\boldsymbol{\Delta}}(\mathbf{x})$ (contour with colormap). We plot their projections along the eigenvectors related to the maximum (a) and minimum (b) eigenvalue of $\mathbf{G}^{-1}(\mathbf{x})$, respectively. Results are expressed on a logarithmic scale.

6.2.3. Bias

Similarly to MSE, Figure 10 illustrates the bias analysis. The first and second rows show the asymptotic prediction $-\frac{1}{2}\mathbf{b}(\mathbf{x})$ and the sample estimate $\widehat{\mathbf{B}}(\mathbf{x})$, respectively. As usual, we project them along the maximum (a) and minimum (b) eigenvectors of $\mathbf{G}^{-1}(\mathbf{x})$. It is important to notice that Algorithms 1 and 2 yields good localization accuracy in both radial and angular components, except for the regions close to the degeneracy locus $\mathbf{D}$. By comparing the simulative results with the prediction of the bias, it is possible to observe a good match, except for the areas where the remainder analysis suggests a relevant error. It is worth noticing that at the points that are far from these areas the bias exhibits very small magnitude, which makes it difficult to estimate its value from simulations. For this reason, the contour lines of expected and simulated values take on different shapes.
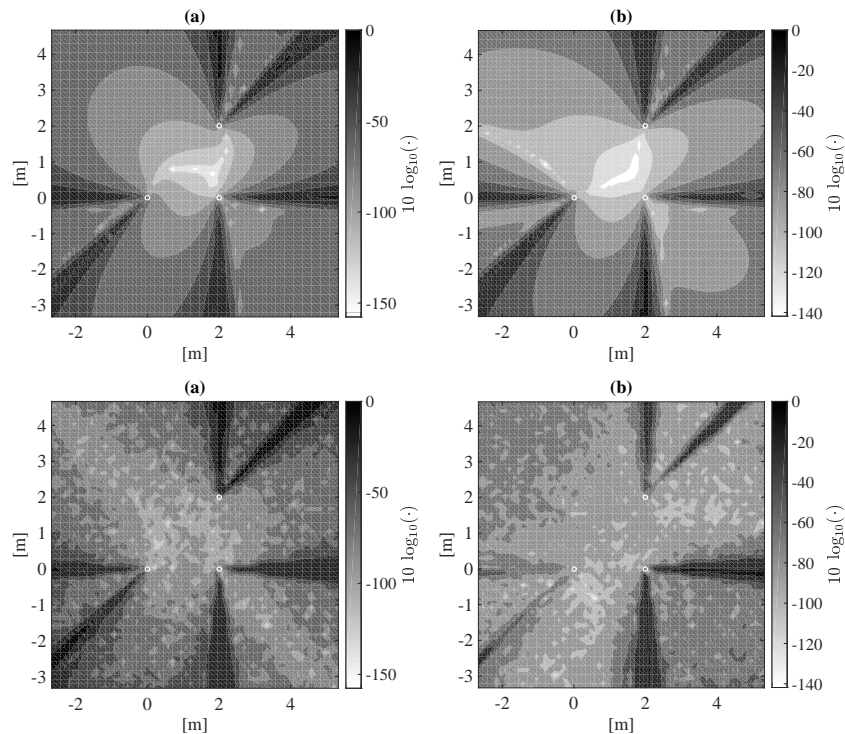
Figure 10: First row: asymptotic prediction $-\frac{1}{2}\mathbf{b}(\mathbf{x})$ according to Equation (36). Second row: sample estimate $\widehat{\mathbf{B}}(\mathbf{x})$ of the bias from simulations. Projections along the eigenvectors related to the maximum (a) and minimum (b) eigenvalue of $\mathbf{G}^{-1}(\mathbf{x})$ are shown. Results are expressed on a logarithmic scale.

6.3. MLE in real scenarios

The analysis we carried out in the previous sections is based on the decomposition of the TDOA–based localization into four different models. In real world situations, the information about the model to choose is available only in particular circumstances, such as in indoor localization where the source lies on a bounded subset of $\mathbb{R}^2$. In general, it is impossible to know which model to use and so it is not possible to avoid the ambiguity of the source localization described in Section 2. This is what we call the *blind* localization scenario.

In the presence of noisy data the situation is rather more complicated. For example, it could happen that data vector $\hat{\boldsymbol{\tau}}$ represents outlier measurements or that $\hat{\boldsymbol{\tau}}$ lies on E^- but it comes from a noisy perturbation of a point in U_i, $i = 0, 1, 2$. In the literature, there exist different ways to address these problems [53, 54]. In this manuscript, we work in the context of statistical hypothesis tests. Let us consider the model M and its parameter set $U \subset \mathbb{R}^2$, being the other cases analogous. Given measurements $\hat{\boldsymbol{\tau}} \in \mathbb{R}^2$, we want to test the null hypothesis H_0 that $\hat{\boldsymbol{\tau}}$ is not an outlier for M versus the alternative H_1 that $\hat{\boldsymbol{\tau}}$ is an outlier. If H_0 holds valid, then $\mathbf{x}_+(\bar{\boldsymbol{\tau}}(\hat{\boldsymbol{\tau}}; \boldsymbol{\Sigma_2}))$ should be seen as an admissible source position, otherwise it should not.

Following usual statistical procedures, one has to define a test statistic and compute its p-value $\xi(\hat{\boldsymbol{\tau}}; \boldsymbol{\tau}, \boldsymbol{\Sigma_2})$ under the null hypothesis. $\xi(\hat{\boldsymbol{\tau}}; \boldsymbol{\tau}, \boldsymbol{\Sigma_2})$ is the probability the statistic is equal or larger than its observed value. Then, fixed a confidence level $\alpha \in [0, 1]$, one accepts $\hat{\boldsymbol{\tau}}$ if $\xi(\hat{\boldsymbol{\tau}}; \boldsymbol{\tau}, \boldsymbol{\Sigma_2}) \geq \alpha$. A natural choice for the test statistic is the squared Mahalanobis distance between $\hat{\boldsymbol{\tau}}$ and the feasible set U [20], that obviously coincides with the distance between $\hat{\boldsymbol{\tau}}$ and $\bar{\boldsymbol{\tau}}(\hat{\boldsymbol{\tau}}; \boldsymbol{\Sigma_2})$. Let us name $\mathcal{X}_n^2$ the Chi–squared distribution with $n > 0$ degrees of freedom, while $\mathcal{X}_0^2$ denotes a Dirac delta on zero. Under H_0, the test statistic follows a mixture of Chi–square distributions:

$$\|\hat{\boldsymbol{\tau}} - \bar{\boldsymbol{\tau}}(\hat{\boldsymbol{\tau}}; \boldsymbol{\Sigma_2})\|^2_{\boldsymbol{\Sigma_2}^{-1}} \sim \beta_0(\boldsymbol{\tau}, \boldsymbol{\Sigma_2}) \, \mathcal{X}_0^2 + \beta_1(\boldsymbol{\tau}, \boldsymbol{\Sigma_2}) \, \mathcal{X}_1^2 + (1 - \beta_0(\boldsymbol{\tau}, \boldsymbol{\Sigma_2}) - \beta_1(\boldsymbol{\tau}, \boldsymbol{\Sigma_2})) \, \mathcal{X}_2^2 \,.$$

The coefficients $\beta_0(\boldsymbol{\tau}, \boldsymbol{\Sigma_2})$ and $\beta_1(\boldsymbol{\tau}, \boldsymbol{\Sigma_2})$ depend on the metric $\boldsymbol{\Sigma_2}$ and the location of the unknown true parameter $\boldsymbol{\tau} \in U$. For a detailled explanation of the problem see [55, 56, 20]. In principle, one could exactly compute these two functions, although this is a very difficult task. Hence, we investigate alternative approaches.

Firstly, let us remark that if $\hat{\boldsymbol{\tau}} \in U$, then $\|\hat{\boldsymbol{\tau}} - \bar{\boldsymbol{\tau}}(\hat{\boldsymbol{\tau}}; \boldsymbol{\Sigma_2})\|^2_{\boldsymbol{\Sigma_2}^{-1}} = 0$ and $\xi(\hat{\boldsymbol{\tau}}; \boldsymbol{\tau}, \boldsymbol{\Sigma_2}) = 1$, therefore H_0 is always accepted. If $\hat{\boldsymbol{\tau}} \notin U$, there exist different strategies depending on the application. For example, one could estimate $\boldsymbol{\tau} = \bar{\boldsymbol{\tau}}(\hat{\boldsymbol{\tau}}; \boldsymbol{\Sigma_2})$ and then numerically evaluate $\beta_0(\boldsymbol{\tau}, \boldsymbol{\Sigma_2})$, $\beta_1(\boldsymbol{\tau}, \boldsymbol{\Sigma_2})$ and $\xi(\hat{\boldsymbol{\tau}}; \boldsymbol{\tau}, \boldsymbol{\Sigma_2})$. Otherwise, a reasonable and computationally cheaper choice is to assume $\boldsymbol{\tau} \in \partial U$ and take global approximations $\beta_0(\boldsymbol{\tau}, \boldsymbol{\Sigma_2}) = \bar{\beta}_0$ and $\beta_1(\boldsymbol{\tau}, \boldsymbol{\Sigma_2}) = \bar{\beta}_1$, with values that best describe the distribution of the squared distances in most situations [20]. This way, the p-value of the test is

$$\xi(\hat{\boldsymbol{\tau}}; \boldsymbol{\tau}, \boldsymbol{\Sigma_2}) = 1 - \left(\bar{\beta}_0 + \bar{\beta}_1 \, F_{\mathcal{X}_1^2} \left(\|\hat{\boldsymbol{\tau}} - \bar{\boldsymbol{\tau}}(\hat{\boldsymbol{\tau}}; \boldsymbol{\Sigma_2})\|^2_{\boldsymbol{\Sigma_2}^{-1}} \right) + \left(1 - \bar{\beta}_0 - \bar{\beta}_1 \right) \, F_{\mathcal{X}_2^2} \left(\|\hat{\boldsymbol{\tau}} - \bar{\boldsymbol{\tau}}(\hat{\boldsymbol{\tau}}; \boldsymbol{\Sigma_2})\|^2_{\boldsymbol{\Sigma_2}^{-1}} \right) \right),$$

where $F_{\mathcal{X}_n^2}$ is the Chi-square cumulative distribution function with n degrees of freedom. In our aid for the choice of $\bar{\beta}_0$ and $\bar{\beta}_1$, there are the following useful approximations:

a) if $\boldsymbol{\tau}$ is on ∂U but sufficiently far from the vertices R_0, R_1, R_2, then one has $\beta_0(\boldsymbol{\tau}, \boldsymbol{\Sigma_2}) \simeq \beta_1(\boldsymbol{\tau}, \boldsymbol{\Sigma_2}) \simeq \frac{1}{2}$;

b) given $\boldsymbol{\tau} = R^i$, let us name $\vartheta_i \in (0, \pi)$ the Mahalanobis angle between the two segments of ∂U having this vertex as common endpoint. If the length of such segments are sufficiently large, one has $\beta_0(R^i, \boldsymbol{\Sigma_2}) \simeq \frac{\vartheta_i}{2\pi}$ and $\beta_1(R^i, \boldsymbol{\Sigma_2}) \simeq \frac{1}{2}$;

c) finally, if the noise is large with respect to the size of the feasible set, one has $\beta_0(\boldsymbol{\tau}, \boldsymbol{\Sigma_2}) \simeq \beta_1(\boldsymbol{\tau}, \boldsymbol{\Sigma_2}) \simeq 0$.

Similar reasoning can be followed for the models M_0, M_1, M_2. Once one identifies all the admissibile source positions, for each of them it is possible to compute the associated error estimation as we explained in Section 5 and validated in this section.

Geometrically speaking, given a significance level α and two mixing probabilities $\bar{\beta}_0$ and $\bar{\beta}_1$, the set of $\hat{\boldsymbol{\tau}}$ for which the null hypothesis is accepted is the offset of the feasible set U at Mahalanobis distance δ such that

$$1 - \left(\bar{\beta}_0 + \bar{\beta}_1 \, F_{\mathcal{X}_1^2} \left(\delta^2 \right) + \left(1 - \bar{\beta}_0 - \bar{\beta}_1 \right) \, F_{\mathcal{X}_2^2} \left(\delta^2 \right) \right) = \alpha. \tag{40}$$

In Figure 11 we draw the four models and their respective regions of acceptance of the data, by setting $\boldsymbol{\Sigma_2} = (0.1 \, d_{10})^2 \, \mathbf{I}$, $\alpha = 0.05$ and $\bar{\beta}_0 = \bar{\beta}_1 = \frac{1}{2}$. By solving Equation (40), in this case we have $\delta \simeq 1.64$. Finally, we summarize all the above discussion in Algorithm 3.
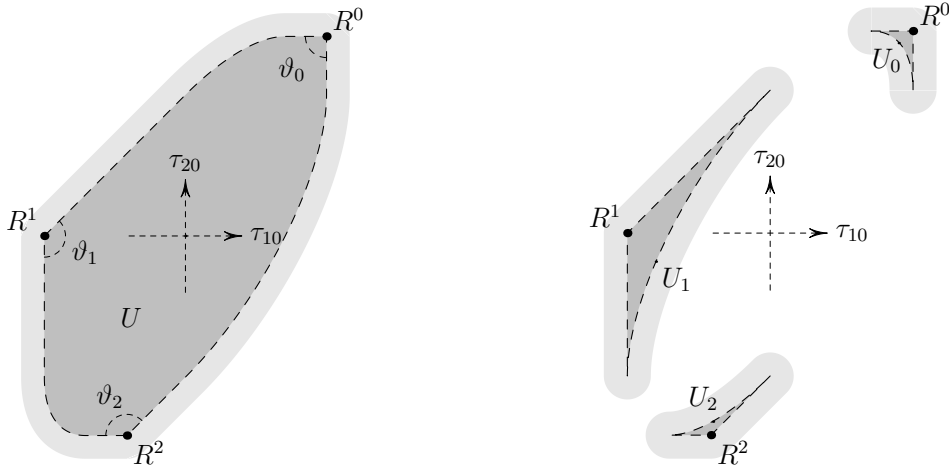

Figure 11: On the left, the medium gray subset is the feasible set U of the model M. On the right, the medium gray subset U_i is the feasible set of the model M_i, $i = 0, 1, 2$. The light gray subsets are the regions of acceptance of the measurements for the various models.

Algorithm 3 MLE algorithm for blind localization
___

Input: TDOA measurements $\hat{\boldsymbol{\tau}}$, covariance matrix $\boldsymbol{\Sigma_2}$, significance thresholds $\delta, \delta_0, \delta_1, \delta_2$

Output: Admissible source positions $\bar{\mathbf{x}}(\hat{\boldsymbol{\tau}}; \boldsymbol{\Sigma_2})$ and $\bar{\mathbf{x}}_{\mathbf{i}}(\hat{\boldsymbol{\tau}}; \boldsymbol{\Sigma_2})$

  1: Compute $\bar{\boldsymbol{\tau}}(\hat{\boldsymbol{\tau}}; \boldsymbol{\Sigma_2})$ and $\bar{\boldsymbol{\tau}}_i(\hat{\boldsymbol{\tau}}; \boldsymbol{\Sigma_2})$, $i = 0, 1, 2$.

  2: If $\|\hat{\boldsymbol{\tau}} - \bar{\boldsymbol{\tau}}(\hat{\boldsymbol{\tau}}; \boldsymbol{\Sigma_2})\|^2_{\boldsymbol{\Sigma_2}^{-1}} < \delta^2$ accept the estimation $\bar{\boldsymbol{\tau}}(\hat{\boldsymbol{\tau}}; \boldsymbol{\Sigma_2})$, else discard the measurements $\hat{\boldsymbol{\tau}}$. The same for $\bar{\boldsymbol{\tau}}_i(\hat{\boldsymbol{\tau}}; \boldsymbol{\Sigma_2})$, $i = 0, 1, 2$.

  3: The admissible source positions are $\bar{\mathbf{x}}(\hat{\boldsymbol{\tau}}; \boldsymbol{\Sigma_2}) = \mathbf{x}_+(\bar{\boldsymbol{\tau}}(\hat{\boldsymbol{\tau}}; \boldsymbol{\Sigma_2}))$ and $\bar{\mathbf{x}}_{\mathbf{i}}(\hat{\boldsymbol{\tau}}; \boldsymbol{\Sigma_2}) = \mathbf{x}_-(\bar{\boldsymbol{\tau}}_i(\hat{\boldsymbol{\tau}}; \boldsymbol{\Sigma_2}))$, $i = 0, 1, 2$, among the ones passing the test in Line 2.
___

7. Conclusions

In this manuscript we studied the statistical model for the Range Difference–based localization, in the minimal scenario of three sensors and a source lying in the plane of the sensors. This analysis arises from previous works [14, 15], where the deterministic model for source localization was described in terms of mapping from the physical space into the measurement space (TDOA space). Our work can be useful in every context where the number of sensors and/or measurements is limited, such as in GPS localization and in applications like the identification of TDOA outliers.

In our investigation, we faced the problem of multiple source location by defining four distinct curved exponential families, one for each region of the physical plane where the TDOA map is injective. On this basis, we developed a Maximum Likelihood technique for localization, which works in the TDOA space and is formulated in a closed-form. Then, we obtained the asymptotical inference of the mean square error and bias on source position, using tools of Information Geometry. We showed via simulation the effectiveness of the proposed MLE algorithms and the quality and accuracy of the asymptotic error prediction. Moreover, we investigated higher order statistics in order to evaluate the reliability of the asymptotic analysis. These instruments are fundamental for treating relevant problems in applications, such as the optimal placements of sensors. These aspects are currently under further investigation.

We conducted the above analysis under the assumption of knowing in advance the statistical model to use, which is not always applicable in a real scenario. In Section 6.3 we proposed an algorithm for source localization that applies to such situations, which is based on the theory of statistical hypothesis tests.

Appendix A. The Mahalanobis degree discriminant

By eliminating ν from system (29) we get the following algebraic equations

$$\begin{cases} \langle \hat{\boldsymbol{\tau}} - \boldsymbol{\tau}, \mathbf{H} \nabla_{\boldsymbol{\tau}} a(\boldsymbol{\tau}) \rangle_{\boldsymbol{\Sigma_2}} = 0 \\ a(\boldsymbol{\tau}) = 0 \end{cases} . \tag{A.1}$$

By Definition 7, the Mahalanobis degree discriminant $\mathcal{E}_{\boldsymbol{\Sigma_2}}$ is the locus of the points $\hat{\boldsymbol{\tau}}$ of the τ–plane where (A.1) has at least two coinciding solutions. This condition is equivalent to require that $\nabla_{\boldsymbol{\tau}} a(\boldsymbol{\tau})$ and $\nabla_{\boldsymbol{\tau}} \langle \hat{\boldsymbol{\tau}} - \boldsymbol{\tau}, \mathbf{H} \nabla_{\boldsymbol{\tau}} a(\boldsymbol{\tau}) \rangle_{\boldsymbol{\Sigma_2}}$ are parallel. A Singular code [51] for computing $\mathcal{E}_{\boldsymbol{\Sigma_2}}$ is:

```
ring r=0,(t1,t2,u,v),lp;
LIB"linalg.lib";
matrix d10[2][1]=d10x,d10y;
matrix d20[2][1]=d20x,d20y;
matrix S[2][2]=s11,s12,s21,s22;
matrix IS=inverse(S);
matrix H[2][2]=0,-1,1,0;
poly a=(d10[1,1]^2+d10[2,1]^2)*t2^2-
2*(d10[1,1]*d20[1,1]+d10[2,1]*d20[2,1])*t1*t2+
(d20[1,1]^2+d20[2,1]^2)*t1^2-
```

```
(d10[1,1]*d20[2,1]-d20[1,1]*d10[2,1])^2;
matrix G[2][1]=diff(a,t1),diff(a,t2);
matrix N=-H*IS*H*G;
matrix MR[2][2]=u-t1,v-t2,N[1,1],N[2,1];
poly R=det(MR);
matrix MT[2][2]=diff(R,t1),diff(R,t2),G[1,1],G[2,1];
poly t=det(MT);
ideal i=a,R,t;
i=std(i);
print(i[1]);
```

The Cartesian equation of $\mathcal{E}_{\Sigma_2}$ is the degree-6 polynomial in `u,v` that is printed thanks to the last line. The only data to be changed are the numerical values `d10x,d10y,d20x,d20y` equal to the components of the displacement vectors and the covariance matrix `S`.

Acknowledgments

References

[1] I. Getting, The Global Positioning System, IEEE Spectrum 30 (12) (1993) 36–47. doi:10.1109/6.272176.

[2] J. Benesty, Y. Huang, Audio Signal Processing for Next-Generation Multimedia Communication Systems, Springer, 2004.

[3] J. Chen, R. Hudson, K. Yao, Maximum-likelihood source localization and unknown sensor location estimation for wideband signals in the near-field, IEEE Transactions on Signal Processing 50 (8) (2002) 1843 –1854. doi:10.1109/TSP.2002.800420.

[4] J. Hu, C. Yang, Estimation of sound source number and directions under a multisource reverberant environment, EURASIP Journal on Advances in Signal Processing 2010 (2010) 1–14. doi:10.1155/2010/870756.

[5] C. Knapp, G. Carter, The generalized correlation method for estimation of time delay, IEEE Transactions on Acoustics, Speech and Signal Processing 24 (4) (1976) 320–327. doi:10.1109/TASSP.1976.1162830.

[6] J. Ianniello, Time delay estimation via cross-correlation in the presence of large estimation errors, IEEE Transactions on Acoustics, Speech and Signal Processing 30 (6) (1982) 998–1003. doi:10.1109/TASSP.1982.1163992.

[7] G. Siouris, Aerospace Avionics Systems, Academic Press, San Diego, 1993.

[8] Z. Yimin, M. Amin, F. Ahmad, Localization of inanimate moving targets using dual-frequency synthetic aperture radar and time-frequency analysis, in: IEEE International Geoscience and Remote Sensing Symposium, 2008. IGARSS 2008, Vol. 2, 2008, pp. II–33–II–36. doi:10.1109/IGARSS.2009.4778920.

[9] K. Yang, G. Wang, Z. Luo, Efficient convex relaxation methods for robust target localization by a sensor network using time differences of arrivals, IEEE Transactions on Signal Processing 57 (7) (2009) 2775–2784. doi:10.1109/TSP.2009.2016891.

[10] D. Li, Y. Hu, Energy-based collaborative source localization using acoustic microsensor array, EURASIP Journal on Advances in Signal Processing 2003 (4) (2003) 321–337. doi:10.1155/S1110865703212075.

[11] S. Spencer, The two-dimensional source location problem for time differences of arrival at minimal element monitoring arrays, Journal of the Acoustical Society of America 121 (6) (2007) 3579–3594. doi:10.1121/1.2734404.

[12] S. Spencer, Closed–form analytical solutions of the time difference of arrival source location problem for minimal element monitoring arrays, Journal of the Acoustical Society of America 127 (5) (2010) 2943–2954. doi:10.1121/1.3365313.

[13] P. Bestagini, M. Compagnoni, F. Antonacci, A. Sarti, S. Tubaro, Tdoa-based acoustic source localization in the space–range reference frame, Multidimensional Systems and Signal Processing 35 (2) (2014) 337–359. doi:10.1007/s11045-013-0233-8.

[14] M. Compagnoni, R. Notari, TDOA-based localization in two dimension: the bifurcation curve, Fundamenta Informaticae 135 (1-2) (2014) 199–210. doi:10.3233/FI-2014-1118.

[15] M. Compagnoni, R. Notari, F. Antonacci, A. Sarti, A comprehensive analysis of the geometry of tdoa maps in localization problems, Inverse Problems 30 (3) (2014) 035004, 1–49. doi:10.1088/0266-5611/30/3/035004.

[16] X. Alameda-Pineda, R. Horaud, A geometric approach to sound source localization from time-delay estimates, IEEE/ACM Transactions on Audio, Speech, and Language Processing 22 (6) (2014) 1082–1095. doi:10.1109/TASLP.2014.2317989.

[17] M. Compagnoni, R. Notari, A. Ruggiu, F. Antonacci, A. A. Sarti, The algebro-geometric study of range maps, Journal of Nonlinear Science 27 (1) (2017) 99–157. doi:10.1007/s00332-016-9327-4.

[18] J. Schicho, M. Gallet, Ambiguities in a problem in planar geodesy, Symmetry, Integrability and Geometry: Methods and Applications 11 (2015) 008, 1–13. doi:10.3842/SIGMA.2015.008.

[19] J. Velasco, D. Pizarro, J. Macias-Guarasa, A. Asaei, Tdoa matrices: Algebraic properties and their application to robust denoising with missing data, IEEE Transactions on Signal Processing 64 (20) (2016) 5242–5254. doi:10.1109/TSP.2016.2593690.

[20] M. Compagnoni, A. Pini, A. Canclini, P. Bestagini, F. Antonacci, S. Tubaro, A. Sarti, A geometrical-statistical approach to outlier removal for tdoa measurements. arXiv:1610.04467.

[21] M. Compagnoni, A. Canclini, P. Bestagini, F. Antonacci, A. Sarti, S. Tubaro, Source localization and denoising: a perspective from the tdoa space, Multidimensional Systems and Signal Processing (2016) 1–26doi:10.1007/s11045-016-0400-9.

[22] S. Amari, H. Nagaoka, Methods of Information Geometry, American Mathematical Society, 2000.

[23] Y. Cheng, X. Wangb, M. Morelande, B. Moran, Information geometry of target tracking sensor networks, Information Fusion 14 (3) (2013) 311–326. doi:10.1016/j.inffus.2012.02.005.

[24] K. C. Ho, Bias reduction for an explicit solution of source localization using tdoa, IEEE Transactions on Signal Processing 60 (5) (2012) 2101–2114. doi:10.1109/TSP.2012.2187283.

[25] H. C. So, Y. T. Chan, K. C. Ho, Y. Chen, Simple formulae for bias and mean square error computation [dsp tips and tricks], IEEE Signal Processing Magazine 30 (4) (2013) 162–165. doi:10.1109/MSP.2013.2254600.

[26] W. Hahn, S. Tretter, Optimum processing for delay-vector estimation in passive signal arrays, IEEE Transactions on Information Theory 19 (5) (1973) 608–614. doi:10.1109/TIT.1973.1055077.

[27] P. Stoica, A. Nehorai, MUSIC, maximum likelihood and cramer-rao bound, in: IEEE International Conference on Acoustics, Speech and Signal Processing (ICASSP), Vol. 4, 1988, pp. 2296–2299. doi:10.1109/ICASSP.1988.197097.

[28] H. Schau, A. Robinson, Passive source localization employing intersecting spherical surfaces from time-of-arrival differences, IEEE Transactions on Acoustics, Speech and Signal Processing 35 (8) (1987) 1223–1225. doi:10.1109/TASSP.1987.1165266.

[29] Y. Huang, J. Benesty, G. Elko, R. Mersereati, Real-time passive source localization: a practical linear-correction least-squares approach, IEEE Transactions on Speech and Audio Processing 9 (8) (2001) 943–956. doi:10.1109/89.966097.

[30] A. Beck, P. Stoica, J. Li, Exact and approximate solutions of source localization problems, IEEE Transactions on Signal Processing 56 (5) (2008) 1770–1778. doi:10.1109/TSP.2007.909342.

[31] R. Schmidt, A new approach to geometry of range difference location, IEEE Transactions on Aerospace and Electronic Systems AES-8 (6) (1972) 821–835. doi:10.1109/TAES.1972.309614.

[32] M. Compagnoni, P. Bestagini, F. Antonacci, A. Sarti, S. Tubaro, Localization of acoustic sources through the fitting of propagation cones using multiple independent arrays, IEEE Transactions on Audio, Speech, and Language Processing 20 (7) (2012) 1964–1975. doi:10.1109/TASL.2012.2191958.

[33] A. Canclini, P. Bestagini, F. Antonacci, M. Compagnoni, A. Sarti, S. Tubaro, A robust and low-complexity source localization algorithm for asynchronous distributed microphone networks, IEEE/ACM Transactions on Audio, Speech, and Language Processing 23 (10) (2015) 1563–1575. doi:10.1109/TASLP.2015.2439040.

[34] J. Draisma, E. Horobet, G. Ottaviani, B. Sturmfels, R. Thomas, The Euclidean distance degree of an algebraic variety, Foundations of Computational Mathematics 16 (1) (2016) 99–149. doi:10.1007/s10208-014-9240-x.

[35] J. Abel, J. Chauffe, Existence and uniqueness of GPS solutions, IEEE Transactions on Aerospace and Electronic Systems 27 (6) (1991) 952–956. doi:10.1109/7.104271.

[36] J. Awange, J. Shan, Algebraic Solution of GPS Pseudo-Ranging Equations, GPS Solutions 5 (4) (2002) 20–32. doi:10.1007/PL00012909.

[37] S. Bancroft, An Algebraic Solution of the GPS Equations, IEEE Transactions on Aerospace Electronic Systems AES-21 (1) (1985) 56–59. doi:10.1109/TAES.1985.310538.

[38] J. Chauffe, J. Abel, On the exact solution of the pseudorange equations, IEEE Transactions on Aerospace and Electronic Systems 30 (4) (1994) 1021–1030. doi:10.1109/7.328767.

[39] B. Coll, J. Ferrando, J. Morales-Lladosa, Positioning systems in minkowski space-time: Bifurcation problem and observational data, Physical Review D 86, 084036 (8) (2012) 1–10. doi:10.1103/PhysRevD.86.084036.

[40] B. Coll, J. Ferrando, J. Morales-Lladosa, Positioning systems in minkowski space-time: from emission to inertial coordinates, Classical Quantum Gravity 27, 065013 (6) (2010) 1–17. doi:10.1088/0264-9381/27/6/065013.

[41] E. Grafarend, J. Shan, GPS Solutions: Closed Forms, Critical and Special Configurations of P4P, GPS Solutions 5 (3) (2002) 29–41. doi:doi:10.1007/PL00012897.

[42] J. Hoshen, The GPS Equations and the Problem of Apollonius, IEEE Transactions on Aerospace and Electronic Systems 32 (3) (1996) 1116–1124. doi:10.1109/7.532270.

[43] J. L. Leva, An alternative closed-form solution to the gps pseudo-range equations, IEEE Transactions on Aerospace and Electronic Systems 32 (4) (1996) 1430–1439. doi:10.1109/7.543864.

[44] J. Picard, A. Weiss, Time difference localization in the presence of outliers, Signal Processing 92 (10) (2012) 2432–2443.

[45] J. Scheuing, B. Yang, Disambiguation of TDOA estimation for multiple sources in reverberant environments, Audio, Speech, and Language Processing, IEEE Transactions on 16 (8) (2008) 1479 –1489. doi:10.1109/TASL.2008.2004533.

[46] R. Kaune, J. Hrst, W. Koch, Accuracy analysis for tdoa localization in sensor networks, in: 14th International Conference on Information Fusion, 2011, pp. 1–8.

[47] D. Cox, J. Little, D. O'Shea, Ideals, Varieties, and Algorithms: An Introduction to Computational Algebraic Geometry and Commutative Algebra, Springer Verlag, New York, 2007.

[48] J. Verschelde, Algorithm 795: Phcpack: A general-purpose solver for polynomial systems by homotopy continuation, ACM Transactions on Mathematical Software 25 (2) (1999) 251–276. doi:10.1145/317275.317286.

[49] D. Bates, J. Hauenstein, A. Sommese, C. Wampler, Numerically solving polynomial systems with Bertini, Vol. 25 of Software, Environments, and Tools, SIAM, Philadelphia, 2013.

[50] S. Friedland, M. Stawiska, Some approximation problems in semi-algebraic geometry, Banach Center Publications 107 (2015) 133–147. doi:10.4064/bc107-0-9.

[51] W. Decker, G.-M. Greuel, G. Pfister, H. Schönemann, SINGULAR 4-1-0 — A computer algebra system for polynomial computations, http://www.singular.uni-kl.de (2016).

[52] N. Higham, Accuracy and Stability of Numerical Algorithms (2nd ed.), SIAM, 2002.

[53] X. Su, P. Shi, L. Wu, Y. D. Song, Fault detection filtering for nonlinear switched stochastic systems, IEEE Transactions on Automatic Control 61 (5) (2016) 1310–1315. doi:10.1109/TAC.2015.2465091.

[54] H. Li, S. Yin, J. Liu, C. Zhao, Novel gaussian approximate filter method for stochastic non-linear system, International Journal of Innovative Computing, Information and Control 13 (1) (2017) 201–218.

[55] H. Chernoff, On the distribution of the likelihood ratio, The Annals of Mathematical Statistics 25 (3) (1954) 573–578. doi:10.1214/aoms/1177728725.

[56] S. G. Self, K. Y. Liang, Asymptotic properties of maximum likelihood estimators and likelihood ratio tests under non-standard conditions, Journal of the American Statistical Association 82 (398) (1987) 605–610. doi:10.2307/2289471.